MASTERARBEIT

Titel der Masterarbeit

Optical readout and control of a levitated dielectric sphere inside a high-finesse cavity

Verfasser

Uroš Delić, BSc

angestrebter akademischer Grad

Master of Science (MSc)

Wien, 2013

Studienkennzahl lt. Studienblatt	A 1048040
Studienrichtung lt. Studienblatt:	A 066 876
Betreuer:	Univ.-Prof. Dr. Markus Aspelmeyer

Acknowledgments

I wish to thank Univ.-Prof. Dr. Markus Aspelmeyer for his guidance and constant help and support during the many years I have spent in his group. His leadership has always been truly inspiring and his hunger for knowledge was always illuminating.

I would especially like to thank to my co-supervisor Dr. Nikolai Kiesel, as this thesis would not see the light of the day without his abundant help and guidance. Discussions about the theoretical model with Sebastian Hofer, as well about the experimental data with swissies Florian Blaser and David Grass were also extremely helpful.

Many other people deserve to be mentioned - the whole Aspelmeyer group has been a great group to be in, and I am looking forward to many future (vegan) group retreats and basketball games.

I think my family takes the most joy in the conclusion of this thesis, and I wish to thank them too for all their exhaustive and loving care over the years I spent in Vienna as a student.

Uroš Delić
Vienna, July 2013.

Abstract

Optically levitated dielectric spheres are of special interest in the field of cavity optomechanics, as they promise unprecedented low mechanical loss. This leads to a high quality factor, which could provide large force sensitivity. Due to the decoupling from thermal environment, experiments in room-temperature quantum optomechanics could also be performed. We present a full theoretical study of the system of a sphere trapped and controlled by two light fields of different powers inside an optical cavity. We derive expressions which describe the harmonic oscillations of the particle in the trap and the coupling of this motion to the light fields. We particularly focus on the detection of the sphere's motion in an actual experiment setup and present the process of data evaluation of the detection. We obtain a set of measurements from a real life experiment, which we use to put some theoretical dependencies to a test.

Zusammenfassung

Optisch levitierte dielektrische Teilchen sind ein vielversprechender Ansatz auf dem Gebiet der Cavity Optomechanik, da sie unerreicht niedrige mechanische Verluste versprechen. Dies führt direkt zu einem hohen Qualitätsfaktor und einer hohen Empfindlichkeit für Kraftmessungen. Durch die Entkopplung von der thermischen Umgebung sollen quantenoptomechanische Experimente auch bei Raumtemperatur möglich werden. Wir präsentieren in dieser Arbeit eine komplette theoretische Untersuchung eines Teilchens, welches durch zwei Lichtfelder verschiedener Intensität innerhalb einer optischen Cavity gefangen und kontrolliert wird. Wir berechnen Gleichungen welche die harmonischen Oszillationen dieses Teilchens in der optischen Falle und die Kopplung seiner Bewegung an das Lichtfeld beschreiben. Wir konzentrieren uns hierbei besonders auf die Messung der Bewegung des Teilchens in einem realistischen experimentellen Aufbau und demonstrieren Verfahren zur Auswertung der gemessenen Signale. Wir benutzen entsprechende experimentelle Daten, um die theoretischen Vorhersagen zu überprüfen.

Contents

1 Introduction

In recent years we have witnessed the expansion of the field of cavity optomechanics, which focuses on the mutual interaction between an optical cavity field and the motion of a mechanical object via radiation pressure [1]. This interaction has been used for the cooling of the object's motion to the ground state [2, 3], as the ground state cooling is a secure way toward the demonstration of the quantum behavior of macroscopic objects, such as the manifestation of the Schrödinger's cat state [4]. The strong coupling has also been demonstrated [5–7], as well as the quantum state control [8, 9].

Although fairly new, the field has already seen quite success with objects of sizes which differ in many orders of magnitude, from atom clouds [10, 11], microtoroids [12] and membranes [13], to a microscopic mirror [14, 15]. More recently, a system consisting of an optically levitated sub-micron dielectric spherical particle in an optical cavity has been proposed, as it was estimated that the center-of-mass motion of the particle would have unprecedented mechanical high quality factors [16–18]. The decoupling from thermal environment promises a large force sensitivity and leads to an experimental regime of room-temperature quantum optomechanics.

In this thesis we commit to study the theory of the interaction between the cavity fields of arbitrary powers and the levitated sub-wavelength sphere, which has already been introduced partially in [19]. In addition, we relate the theoretical model to a real life experiment [20], by using it for evaluation and modeling of the data, hence putting the theoretical model to a test.

We start by reviewing the basic concepts of damped driven harmonic oscillators and of optical cavities in Chapter 2, which will be useful later in the discussion of the particle's motion in a cavity. The theoretical model of the system is introduced in Chapter 3, where we write the total Hamiltonian of the system and show the oscillatory behavior of the particle's motion. We further focus on the particle's frequency and the optomechanical coupling between its motion and the light fields. We proceed by deriving the Langevin equations of motion, which we solve in Chapter 4 and we infer the noise power spectrum of the particle's motion. We then concentrate on the real life experiment detection technique, which we describe in Chapter 5. We show a successful extraction of the particle's motion from the detected noise power spectrum in Chapter 6, which we use to test the theoretical model of the system.

2 Basic principles of mechanics and cavities

The underlying physical process in our experiment is the interaction of two cavity fields with a particle, which includes trapping in the harmonic potential and controlling the motion of the particle. Hence, we first provide a concise overview of the necessary equations that govern the behavior of classical harmonic oscillators and optical cavities.

2.1 Classical harmonic oscillator

One of the most examined systems in physics is the harmonic oscillator. Its behavior is governed by the following differential equation:

$$\ddot{x} + \gamma \dot{x} + \Omega^2 x = f(t), \tag{2.1}$$

where $f(t) = \frac{F(t)}{m}$, m being the mass of the oscillator and $F(t)$ being the driving force of the oscillator. Ω is the oscillator's frequency and γ is the damping coefficient, sometimes also called the decay rate of the oscilator. In the absence of an external force, i.e. $F(t) = 0$, the (homogeneous) solution to the equation (2.1) is:

$$x_{ho}(t) = Ae^{-\frac{\gamma}{2}t} \sin\left(\sqrt{\Omega^2 - \frac{\gamma^2}{4}}t + \varphi\right), \tag{2.2}$$

where φ is the phase and A is the amplitude of the oscillations, which is given by the initial conditions. Equation (2.2) clearly shows the decaying behavior of the oscillator's motion with the decay rate $\gamma/2$.

Let us now consider a sinusoidal external driving force:

$$f(t) = \frac{F_0}{m} \sin(\omega_0 t), \tag{2.3}$$

where F_0 is the amplitude of the force and ω_0 is the driving frequency. The (heterogeneous) solution to equation (2.1) is:

$$x_{he}(t) = B \sin\left(\omega_0 t + \varphi\right), \tag{2.4}$$

with amplitude B and phase φ being:

$$B = \frac{F_0/m}{\sqrt{(\Omega^2 - \omega_0^2)^2 + \omega_0^2\gamma^2}}, \tag{2.5a}$$

$$\varphi = \arctan \frac{-\omega_0\gamma}{\Omega^2 - \omega_0^2}. \tag{2.5b}$$

The general solution of the equation (2.1) in the Fourier space is:

$$\tilde{x}(\omega) = \frac{\tilde{F}(\omega)}{m} \frac{1}{\Omega^2 - \omega^2 + i\omega\gamma}, \tag{2.6}$$

where $\tilde{F}(\omega)$ is the Fourier transform of force $F(t)$, while the oscillator's susceptibility is defined as:

$$\chi(\omega) = \frac{1}{\Omega^2 - \omega^2 + i\omega\gamma}. \tag{2.7}$$

We can evaluate the noise power spectrum (NPS) of $x(t)$, given by (Appendix 8.A):

$$S_{xx}(\omega)\delta(\omega + \omega') = \langle \tilde{x}(\omega)\tilde{x}^*(\omega') \rangle. \tag{2.8}$$

If the oscillator is coupled to an external bath at temperature T, it is driven by Brownian noise $\eta(t)$, which acts as a random stochastic driving force. The force can be described as an infinite sum of driving forces from equation (2.3) with equal driving amplitudes and all possible frequencies. The force satisfies the correlation property [16]:

$$\langle \eta(t)\eta(t') \rangle = 2\gamma m k_B T \delta(t - t'). \tag{2.9}$$

This expression can be used to obtain the NPS S_{xx} of the $x(t)$:

$$S_{xx} = \frac{2k_B T}{m} \frac{\gamma}{(\Omega^2 - \omega^2)^2 + (\gamma\omega)^2}, \tag{2.10}$$

with $\langle \tilde{\eta}(\omega)\tilde{\eta}^*(\omega') \rangle = 2\gamma m k_B T \delta(\omega + \omega')$. In order to explore the resonance of this solution, we solve the equation:

$$(\Omega^2 - \omega^2)^2 + (\gamma\omega)^2 = 0,$$

which gives four solutions for the frequency ω:

$$\omega_{1,2,3,4} = \frac{\pm i\gamma \pm \sqrt{4\Omega^2 - \gamma^2}}{2}. \tag{2.11}$$

Both the real and complex part of ω have physical meaning. The real part of ω is the actual frequency, while the complex part corresponds to the total damping of the oscillator. Apparently, the change in oscillator's behavior occurs around $\gamma/2\Omega = 1$, which is called the critically damped oscillator. In this case, ω is an imaginary number, and the oscillator decays from the starting amplitude to zero with the damping rate $\gamma/2$. The case of $\gamma/2\Omega > 1$ is called the over-damped harmonic oscillator. The total damping is then greater than $\gamma/2$, and the oscillator decays even faster to zero.

The regime when $\gamma/2\Omega < 1$ describes the under-damped harmonic oscillator, where the damping is $\gamma/2$ and the resonant frequency can be obtained as the real part of the solution for frequency ω:

$$\omega_r = \sqrt{\Omega^2 - \frac{\gamma^2}{4}}. \tag{2.12}$$

Along with the ratio $\frac{\gamma}{2\Omega}$, the quality factor is also in use:

$$Q = \frac{\Omega}{\gamma}. \tag{2.13}$$

The quality factor represents the ratio of the total energy of the oscillator and oscillator's energy loss during one period of oscillations. Hence, the oscillator doesn't make a full oscillation in the over-damped and critically damped regime.

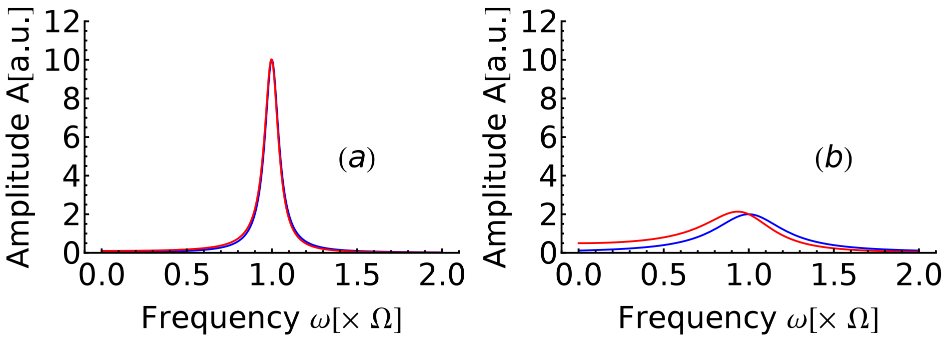

Figure 2.1: **Comparison of S_{xx} (red curve) and S_L (blue curve)**. Spectrum of the harmonic oscillator S_{xx} for small γ can be approximated by the Lorentzian distribution S_L. However, for big γ, one needs to continue using the expression S_{xx}. (a) Comparison of two spectral functions for $\Omega = 1$, $\gamma = 0.1$. The functions almost completely overlap and there is no obvious difference neither in the center frequency nor in the peak width. (b) Comparison of two spectral functions for $\Omega = 1$, $\gamma = 0.5$. One can see a clear discrepancy in both the center frequency and the width of the peaks. Opposite to S_L, function S_{xx} is not symmetric around the center frequency.

It is also interesting to consider the case when γ is small, i.e. when the spectrum S_{xx} is localized around Ω. We can make an approximation $\omega \approx \Omega$ (Figure 2.1), which gives the known Lorentzian spectrum:

$$S_L = \frac{k_B T}{m\Omega^2} \frac{\gamma/2}{(\Omega-\omega)^2 + \left(\frac{\gamma}{2}\right)^2}.$$

The time-average of the oscillator's position $\langle x(t) \rangle$ is zero. However, the mean square displacement $\langle |x(t)|^2 \rangle$ is not zero and can be obtained from the Wiener-Khinchin theorem:

$$\langle |x(t)|^2 \rangle = \frac{1}{2\pi} \int_{-\infty}^{+\infty} S_{xx}(\omega) d\omega = \frac{k_B T}{m\Omega^2}. \tag{2.14}$$

Note that this recovers the equipartition theorem.

2.2 Optical cavity

An optical cavity or resonator is used to enhance the light power in some region of space, which makes it desirable in quantum optics, where a strong interaction between light and an arbitrary object is needed. For the following discussion we consider a Fabry-Perot optical cavity, which consists of two opposite flat mirrors on some distance L (Figure 2.2). When the light frequency becomes resonant to L, a standing wave is created inside the cavity, while some light is transmitted through it. Other optical cavities include curved mirrors in their design, where the created standing wave has a changing intensity beam profile along the cavity axis. We provide here only a short outline of the relevant facts about optical cavities. We first focus only on the longitudinal modes, i.e. on the conditions for the formation of a standing wave, and then we proceed to discuss the transverse modes in an optical cavity with curved mirrors.

Let us assume that the light comes to the Fabry-Perot cavity mirror with reflectivity $R_1 < 1$, as shown in Figure 2.2. The non-zero transmission T_1 ensures that some light passes into the optical cavity. Once inside, most of the light bounces from mirror to mirror due to high mirror reflectivities. Some part transmits through the second mirror though, and subsequent interference of all reflection and transmission paths results in the overall transmission of the optical cavity [21]:

$$\mathcal{T} = \frac{1}{1 + \frac{4\mathcal{F}^2}{\pi^2}\sin^2(\phi/2)}, \tag{2.15}$$

where ϕ is the phase the light accumulates during one round-round trip in the cavity, given by:

$$\phi = \frac{4\pi L}{\lambda}. \tag{2.16}$$

L is the distance between the mirrors, i.e. the cavity length, while λ is the light wavelength. $\mathcal{F}$ is called the optical finesse, and can be calculated from the mirror reflectivities:

$$\mathcal{F} = \frac{\pi (R_1 R_2)^{1/4}}{1 - \sqrt{R_1 R_2}}. \tag{2.17}$$

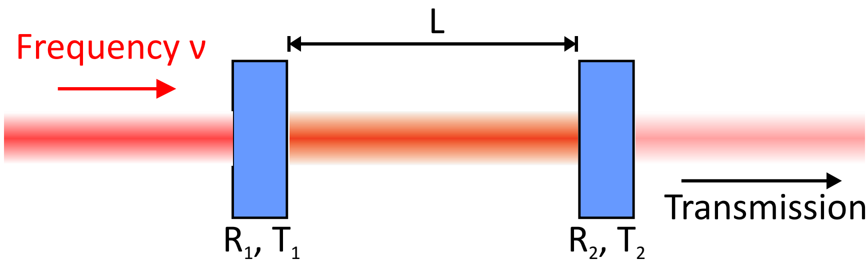

Figure 2.2: **Fabry-Perot optical cavity**. Fabry-Perot optical cavity is composed of two planar mirrors, separated by cavity length L. Mirrors can have different reflectivities R_1, R_2 and transmittivities T_1, T_2. Light is transmitted through the cavity when the light frequency ν is close to one of the cavity resonances $\nu_{\text{res}} = n\frac{c}{2L}$.

We can see from equation (2.15) that the cavity transmission is always $\mathcal{T} \leq 1$. It can reach $\mathcal{T} = 1$ when $\sin^2(\phi/2) = 0$, which is satisfied when the cavity length is equal to an integer number n of half wavelengths:

$$L = n\frac{\lambda}{2}, \tag{2.18}$$

When this condition is satisfied, the light frequency is on the resonance with the cavity, and the standing wave is created inside the cavity. The resonant frequency of light is $\nu_{\text{res}} = n\frac{c}{2L}$ (c - speed of light), while the spacing between two successive resonant frequencies is given by the free spectral range frequency (FSR):

$$FSR = \frac{c}{2L}. \tag{2.19}$$

Figure 2.3 shows the transmission in dependence of the light frequency, where we see the resonances as equally spaced peaks. The peaks have a non-zero width due to the non-zero transmittivity of mirrors. The cavity intensity total decay rate κ is the half width at half maximum (HWHM):

$$\kappa = \frac{\pi c}{\mathcal{F} L}. \tag{2.20}$$

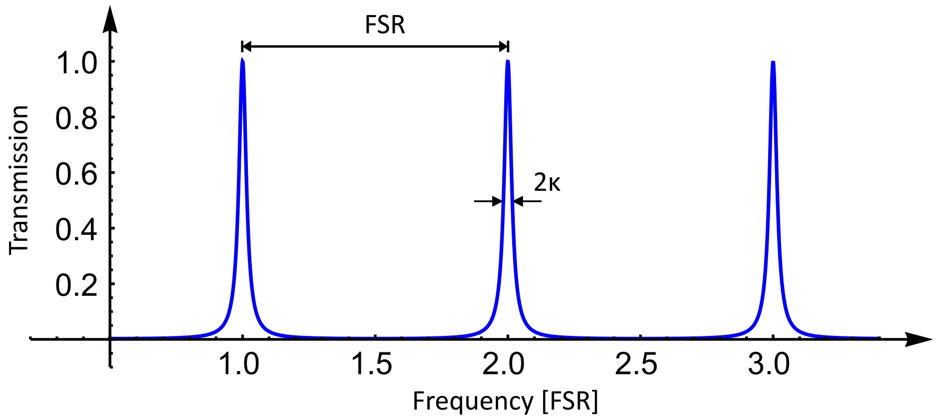

Figure 2.3: **Cavity transmission in dependence of the light frequency**. Cavity transmission shows the multiple cavity resonances, each with the frequency being an integer multiple of the free spectral range (FSR) frequency and the HWHM κ. The mirror reflectivities were taken to be the same $R_1 = R_2 = 0.9$, thus setting the finesse $\mathcal{F} \approx 30$.

The electric field of a standing wave in the Fabry-Perot cavity oscillates as:

$$E(x) = E_0 \sin(kx), \tag{2.21}$$

where we have taken the optical axis to be x-axis, with $x = 0$ set at the mirror where light enters the cavity. E_0 is the amplitude of the electric field and $k = \frac{2\pi}{\lambda}$ is the light wavevector. Hence the light intensity is:

$$I(x) = \frac{c\varepsilon_0}{2} E_0^2 \sin^2(kx). \tag{2.22}$$

In the case of curved mirrors, the cavity transverse mode takes a Gaussian shape [22]:

$$I(x,y,z) = \frac{c\varepsilon_0}{2} E_0^2 \sin^2(kx) \left(\frac{w_0}{w(x)}\right)^2 \exp\left[-2\frac{y^2+z^2}{w^2(x)}\right], \tag{2.23}$$

where w_0 is the minimum value of the beam waist, and $w(x)$ is the beam waist dependence of the position in the cavity x:

$$w(x) = w_0 \sqrt{1 + \left(\frac{x - x_0}{x_R}\right)^2}. \tag{2.24}$$

x_0 is the position where the waist of the mode is w_0 and x_R is called the Rayleigh range:

$$x_R = \frac{\pi w_0^2}{\lambda}. \tag{2.25}$$

3 Optomechanical interaction

Optomechanics deals with the interaction between a cavity light field and the mechanical motion of different objects, usually modelled by a harmonic oscillator. A common example of an optomechanical system is an optical cavity, where one of the mirrors is a harmonic oscillator [14, 15]. This mirror has a constant resonant mechanical frequency, set by the mirror geometry. Building on the proposals [16, 17], we have created an experiment which explores the interaction between a levitated dielectric sphere and two optical fields of different strengths in a cavity.

The sketch of a theoretical model has already been given in [19]. Here we present a full theoretical model, which we apply to a real life experiment [20]. We start by exploring the Hamiltonian in detail, which we will use to recover the equations of motion of the system.

3.1 Hamiltonian

The system essentially consists of a spherical particle interacting with two fields in an optical cavity. Two relevant longitudinal resonances of the cavity are considered, driven by the two beams. The driving frequencies of two beams are related by $\omega_c^1 = \omega_c^2 + FSR$, where FSR (free spectral range) is defined as $FSR = \frac{c}{2L}$, with L being the cavity length. In the most general case, those two resonances are driven by light fields that are detuned from the respective resonances by Δ_1 and Δ_2. The full Hamiltonian expression can be written as a sum of the following free parts (superscript f), driving parts of the fields (superscript d) and interaction parts (superscript i) between the mechanics (subscript m) and the fields (subscripts 1 and 2 for two fields):

$$\hat{H} = \hat{H}_1^f + \hat{H}_2^f + \hat{H}_m^f + \hat{H}_{m1}^i + \hat{H}_{m2}^i + \hat{H}_1^d + \hat{H}_2^d, \tag{3.1}$$

where each term belongs to:

$\hat{H}_1^f$: first beam cavity mode

$\hat{H}_2^f$: second beam cavity mode

$\hat{H}_m^f$: the kinetic energy of the particle

$\hat{H}_{m1}^i$: interaction between the particle and the first beam

$\hat{H}^i_{m2}$: interaction between the particle and the second beam
$\hat{H}^d_1$: driving of the first beam's cavity mode
$\hat{H}^d_2$: driving of the second beam's cavity mode

We focus now on each part of the Hamiltonian in more detail.

3.1.1 Free Hamiltonians

Hamiltonians $\hat{H}^f_1$, $\hat{H}^f_2$, $\hat{H}^d_1$ and $\hat{H}^d_2$ come solely from the interaction of the external light field with the optical cavity. Quantization of an electromagnetic field in an optical cavity is a well known procedure and covered in great detail in textbooks, such as [23]. As such, we assert that it is common knowledge, so we start from the quantized single mode electric field, propagating only along the cavity axis x, which can be separated into a positive frequency part $E^+(t)$ and a negative frequency part $E^-(t)$:

$$E^+(t) = \left(\frac{\hbar\omega}{2\varepsilon_0 V}\right)^{1/2} \hat{a} e^{-i\omega t}, \tag{3.3a}$$

$$E^-(t) = \left(\frac{\hbar\omega}{2\varepsilon_0 V}\right)^{1/2} \hat{a}^\dagger e^{i\omega t}, \tag{3.3b}$$

where V is the cavity mode volume. Operators $\hat{a}$ and $\hat{a}^\dagger$ are light annihilation and creation operators of the light quantum harmonic oscillator (QHO), respectively. Light frequency ω is resonant to the optical cavity. Hamiltonians $\hat{H}^f_1$ and $\hat{H}^f_2$ are then:

$$\hat{H}^f_1 = \hbar\omega^1_c \left(\hat{a}^\dagger_1 \hat{a}_1 + \frac{1}{2}\right), \tag{3.4a}$$

$$\hat{H}^f_2 = \hbar\omega^2_c \left(\hat{a}^\dagger_2 \hat{a}_2 + \frac{1}{2}\right). \tag{3.4b}$$

Factors $\frac{1}{2}\hbar\omega^{1,2}_c$ can be neglected as they don't have any dynamical effect on the system under study.

The driving Hamiltonians $\hat{H}^d_1$ and $\hat{H}^d_2$ come from the interaction between the driving, external field and the cavity mode field [24]:

$$\hat{H}^d_{\text{int}} = i\hbar \int\limits_{-\infty}^{+\infty} d\omega \sqrt{2\kappa}[b(\omega)a^\dagger - b^\dagger(\omega)a], \tag{3.5}$$

where κ is the cavity HWHM, while $b(\omega)$ and $b^\dagger(\omega)$ are annihilation and creation operators of the driving external light field, respectively. By simple transformations, we get to the expressions:

$$\hat{H}_1^d = iE_1(\hat{a}_1^\dagger e^{-i\Omega_1 t} - \hat{a}_1 e^{i\Omega_1 t}), \tag{3.6a}$$
$$\hat{H}_2^d = iE_2(\hat{a}_2^\dagger e^{-i\Omega_2 t} - \hat{a}_2 e^{i\Omega_2 t}). \tag{3.6b}$$

E_1 and E_2 depend on the driving power $P_{1,2}$:

$$E_{1,2} = \sqrt{\frac{2P_{1,2}\kappa}{\hbar\Omega_{1,2}}}. \tag{3.7}$$

The kinetic energy of the particle is equal to:

$$\hat{H}_m^f = \frac{\hat{p}_m^2}{2m}, \tag{3.8}$$

which is just the energy of a free particle with mass m. The harmonic potential energy comes from the interaction with the light fields and it is a part of Hamiltonians $\hat{H}_{m1}^i$ and $\hat{H}_{m2}^i$, which we will study in more detail below.

3.1.2 Dipole interaction

A dielectric sphere can be polarized by applying an electric field. For a sphere that is much smaller than the wavelength (Rayleigh regime), the optical electric field can be assumed to be uniform, i.e. it doesn't change over the distances of the particle diameter. The ratio of the induced dipole moment p and the electric field E_0 at the particle, which induces its dipole moment, is defined as polarizability α:

$$p = \alpha E_0.$$

The polarizability can be obtained by solving the Laplace equation for the electric potential in and out of the sphere (see Appendix 8.B for detailed derivation):

$$\alpha = 3\varepsilon_0 V \frac{\varepsilon_1 - \varepsilon_2}{\varepsilon_1 + 2\varepsilon_2}.$$

The polarizability depends on the sphere's volume V, permittivity of vacuum ε_0, relative permittivity of the sphere ε_1 and relative permittivity of the medium surrounding the sphere ε_2. In this thesis, all experiments are done in air or vacuum, so we can take $\varepsilon_2 = 1$.

The potential energy of a dipole interaction is given by:

$$W = -\vec{p} \cdot \vec{E} = -\alpha|E|^2.$$

$|E|^2$ is related to the light intensity at the particle's position. In the case of two orthogonally polarized electric fields with amplitudes E_1 and E_2, we have $|E|^2 = |E_1|^2 + |E_2|^2$ and the interaction between the light fields and the sphere can be set apart:

$$W = H^i_{m1} + H^i_{m2} = -\alpha|E_1|^2 - \alpha|E_2|^2.$$

The electric field operator of cavity fields $j = 1, 2$ is quantized as $E^+_j(\vec{r}) = \sqrt{\frac{\hbar\omega_j}{2\varepsilon_0 V_c}} f_j(\vec{r}) a^\dagger_j$, where $f_j(\vec{r})$ is the mode function of the field, ω_j is the mode frequency and V_c is the cavity mode volume. This gives the following field-sphere interaction [25]:

$$H^i_{mj} = -\alpha E^+ E^- = -\hbar U_0 \left|f_j(\vec{r})\right|^2 \hat{a}^\dagger_j \hat{a}_j, \tag{3.9}$$

where we have assumed that the field frequencies ω_1 and ω_2 are approximately equal and introduced the constant $U_0 = \frac{\omega_{1,2}\alpha}{2\varepsilon_0 V_c}$. The cavity mode $\left|f_j(\vec{r})\right|^2$ has an envelope of a Gaussian beam, given by (2.23). We can take the slowly changing Gaussian mode shape from the fast-changing standing wave dependence on the position along the cavity axis x into the constant U_0:

$$U_0(x) = \frac{\omega_j \alpha}{2\varepsilon_0 V_c} \left(\frac{w_0}{w(x)}\right)^2. \tag{3.10}$$

The interaction Hamiltonian can then be written as:

$$H^i_{mj} = -\hbar U_0(x) \sin^2(k_j x) \hat{a}^\dagger_j \hat{a}_j. \tag{3.11}$$

3.1.3 Study of the Hamiltonian

The goal in the end is to obtain the equations which show the behavior of the system variables, i.e. the equations of motion. We start by writing the total Hamiltonian for the system in the optical cavity. We then apply procedures to simplify the Hamiltonian, which will give the harmonic potential that causes the particle's oscillatory behavior.

Taking into account the expressions for the contributions to the Hamiltonian from equations (3.4), (3.6), (3.8) and (3.11) leads to the expression for the total Hamiltonian:

$$\begin{aligned} \hat{H}/\hbar &= \omega^1_c \hat{a}^\dagger_1 \hat{a}_1 + \omega^2_c \hat{a}^\dagger_2 \hat{a}_2 + \frac{\hat{p}^2_m}{2m\hbar} - U_0 \hat{a}^\dagger_1 \hat{a}_1 \sin^2(k_1 \hat{x}) - U_0 \hat{a}^\dagger_2 \hat{a}_2 \sin^2(k_2 \hat{x}) \\ &\quad + iE_1(\hat{a}^\dagger_1 e^{-i\Omega_1 t} - \hat{a}_1 e^{i\Omega_1 t}) + iE_2(\hat{a}^\dagger_2 e^{-i\Omega_2 t} - \hat{a}_2 e^{i\Omega_c t}). \end{aligned} \tag{3.12}$$

By applying the unitary operator $\hat{U} = e^{i\Omega_1 \hat{a}^\dagger_1 \hat{a}_1 t} + e^{i\Omega_2 \hat{a}^\dagger_2 \hat{a}_2 t}$ to the Hamiltonian, we transform the parts of Hamiltonian featuring the fields in rotating frames of the respective fields. This makes two important changes to the Hamiltonian: the exponential functions of time from the driving terms of the cavity are eliminated, and the detunings $\Delta_{1,2} = \Omega_{1,2} - \omega_c^{1,2}$ feature in the cavity energy rather than the cavity resonance frequencies. Frequencies $\Omega_{1,2}$ here represent the real frequencies of the light beams. The unitary operator also transforms the operators $\hat{a}_1$ and $\hat{a}_2$. In total, the Hamiltonian is transformed into:

$$\begin{aligned}\hat{H}/\hbar \;&=\; -\Delta_1\hat{a}_1^\dagger\hat{a}_1 - \Delta_2\hat{a}_2^\dagger\hat{a}_2 + \frac{\hat{p}_m^2}{2m\hbar} - U_0\hat{a}_1^\dagger\hat{a}_1\sin^2(k_1\hat{x}) \\ &\quad -U_0\hat{a}_2^\dagger\hat{a}_2\sin^2(k_2\hat{x}) + iE_1(\hat{a}_1^\dagger - \hat{a}_1) + iE_2(\hat{a}_2^\dagger - \hat{a}_2), \end{aligned} \tag{3.13}$$

In the experiment, cavity field frequencies are of the order of 10^{14} Hz, which is many orders of magnitude larger than the FSR ($\approx$ 13.7 GHz). Hence, we can assume that $k_2 - k_1 \ll k_2$. This can be used in $\sin^2(k_2\hat{x}) = \sin^2\left(k_1\hat{x} + (k_2 - k_1)\hat{x}\right)$, as we can think of $(k_2 - k_1)\hat{x}$ as a position-dependent phase difference between the two beams:

$$\varphi = (k_2 - k_1)x_s = \frac{2\pi FSR}{c}x_s = \frac{\pi}{L}x_s, \tag{3.14}$$

where $x_s = \langle\hat{x}\rangle$. From this point on, we write k instead of k_1, as we have effectively eliminated k_2. The position operator $\hat{x}$ can be further expressed as a sum of the steady state value x_s and a new position operator describing just the fluctuation $\hat{x}_m$. In the quantum mechanical description, this fluctuation can be expressed in terms of annihilation and creation operators of the quantum harmonic oscillator (Appendix 8.C):

$$\hat{x}_m = \frac{1}{\sqrt{2}}X_{gs}(\hat{b} + \hat{b}^\dagger), \tag{3.15}$$

where X_{gs} is the ground state extension. The definition of the new position operator makes it possible to perform a Taylor expansion of $\sin^2 k_j\hat{x}$ around x_s:

$$\sin^2 k_j\hat{x} = \sin^2(k_jx_s) + k_j\sin(2k_jx_s)\cdot\hat{x}_m + k_j^2\cos(2k_tx_s)\cdot\hat{x}_m^2.$$

We can also expand the light field operators $\hat{a}$ around their steady state values, defined by $\alpha_j = \langle\hat{a}_j\rangle_t$. Variable α_j can be complex and its complex phase ϕ_j depends on the detuning Δ_j, which we show in the following sections. By applying a final rotation of the light operator, we ensure that the steady state value α_j becomes real. After applying the rotation and the displacement of the operator by $\hat{a}_j^{old} = (\hat{a}_j^{new} + \alpha_j)e^{i\phi_j}$, we get:

$$\hat{a}_j^{old,\dagger}\hat{a}_j^{old} = \alpha_j^2 + \alpha_j(\hat{a}_j^{new,\dagger} + \hat{a}_j^{new}) + \hat{a}_j^{new,\dagger}\hat{a}_j^{new}.$$

Previous consideration of the mechanics operator and the light operators can be implemented to simplify the Hamiltonian:

$$\frac{H}{\hbar} = -(\Delta_1 + U_0\sin^2(kx_s))(\alpha_1^2 + \alpha_1(\hat{a}_1 + \hat{a}_1^\dagger) + \hat{a}_1^\dagger\hat{a}_1) \tag{3.16a}$$

$$- (\Delta_2 + U_0 \sin^2(kx_s + \varphi))(\alpha_2^2 + \alpha_2(\hat{a}_2 + \hat{a}_2^\dagger) + \hat{a}_2^\dagger \hat{a}_2) \tag{3.16b}$$

$$- 2U_0 k^2 \alpha_1^2 \cos(2kx_s)\frac{\hat{x}_m^2}{2} - 2U_0 k^2 \alpha_2^2 \cos(2kx_s + 2\varphi)\frac{\hat{x}_m^2}{2} + \frac{\hat{p}_m^2}{2m\hbar} \tag{3.16c}$$

$$- U_0 k \left(\alpha_1 \sin(2kx_s)(\hat{a}_1 + \hat{a}_1^\dagger) + \alpha_2 \sin 2(kx_s + \varphi)(\hat{a}_2 + \hat{a}_2^\dagger)\right)\hat{x}_m \tag{3.16d}$$

$$- U_0 \alpha_1^2 k \sin(2kx_s))\hat{x}_m - U_0 \alpha_2^2 k \sin 2(kx_s + \varphi)\hat{x}_m \tag{3.16e}$$

$$+ iE_1(\hat{a}_1^\dagger e^{-i\phi_1} - \hat{a}_1 e^{i\phi_1}) + iE_c(\hat{a}_2^\dagger e^{-i\phi_2} - \hat{a}_2 e^{i\phi_2}). \tag{3.16f}$$

Some interesting implications can be analyzed already from this Hamiltonian. For example, it contains the dynamical behavior of the nanoparticle and light fields, so the constant terms can be immediately neglected. Parts (3.16a) and (3.16b) show us that there is a shift in the detuning frequencies of the light field, as well as in the cavity resonance frequencies. This frequency shift is induced by the presence of a particle in the cavity, which depends on the constant U_0 and the position in the cavity. In the experiment, we continuously follow the overall detuning of the light fields, which keeps these shifts invisible to us. One beam is always resonant to the optical cavity, and thus the condition $\Delta_1 + U_0 \sin^2(kx_s) = 0$ is always satisfied. The second beam still has arbitrary detuning, so it makes sense to write $\Delta_2 + U_0 \sin^2(kx_s + \varphi) = \Delta_2$. We also keep the ratio of powers of the two beams, i.e. the ratio of α_2^2 and α_1^2 stable and equal to a set value μ:

$$\frac{\alpha_2^2}{\alpha_1^2} = \mu. \tag{3.17}$$

Line (3.16c) has the structure of $\frac{1}{\hbar}\left(\frac{m\Omega_m^2 \hat{x}_m^2}{2} + \frac{\hat{p}_m^2}{2m}\right)$, which is a known expression for the total energy of a harmonic oscillator. Evidently, we can express the particle's oscillation frequency Ω_m as:

$$\Omega_m^2 = -\frac{2\hbar U_0 k^2}{m}\left(\alpha_1^2 \cos(2kx_s) + \alpha_2^2 \cos(2kx_s + 2\varphi)\right). \tag{3.18}$$

Therefore, the harmonic oscillator behavior of the particle comes from the dipole interaction. In the case when $\mu = 0$, just the resonant cavity field exists and creates the harmonic potential, where the particle is trapped. The particle is trapped in the potential minimum (but intensity maximum) $x_s = x_0$, which is satisfied when $\cos(2kx_0) = 1$. For non-zero μ, the combined two-field potential depends on the phase φ. The overall potential minimum x_s can be found by finding a root of the first derivative of Ω_m^2, which depends on μ and φ:

$$\tan(2kx_s) = -\frac{\mu \sin(2\varphi)}{1 + \mu \cos(2\varphi)}. \tag{3.19}$$

In the regime when $\mu < 1$, the trapping is predominantly done by the resonant cavity field. In this regime, the second beam is primarily used as a fine control of the particle's motion, which we will see in the following text. We proceed by naming the first and the second field a trapping (index t) and control field (index c), respectively. Figure 3.1 is an example of the combined trapping by the two beams with power ratio $\mu = 0.4$ and some phase shift μ.

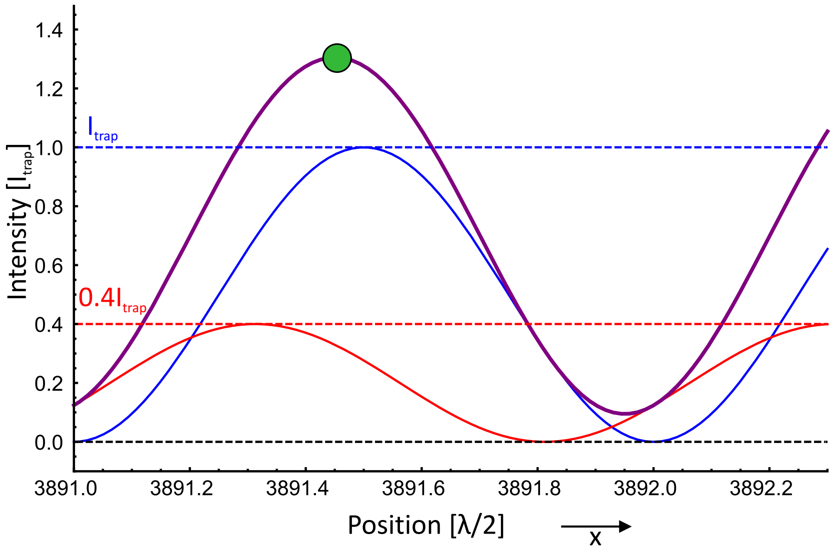

Figure 3.1: **Particle trapped in the overall intensity maximum of two superimposed cavity modes.** Trapping (blue line) and control (red line) cavity mode, with frequencies differing by a FSR, superimpose (violet line) to trap a particle (green circle) in the common intensity maximum. Due to different frequency, two beams have maxima at different positions. At the ratio between the maximum intensity of control (red dashed line) and trapping beam (blue dashed line) being already 0.4, the total maximum is not far away from the maximum of the trapping beam. The particle sees the linear gradient of the control field intensity, which leads to linear coupling.

Line (3.16d) consists of terms of the shape $(\hat{a}_j^\dagger + \hat{a}_j)(b^\dagger + b)$, which are the coupling terms between the particle's motion and the light in the cavity. Single photon coupling constants between the light fields and the mechanical oscillator are defined as the constants in those terms:

$$g_t = \zeta_t \cdot X_{gs} = U_0 k X_{gs} \sin(2kx_s) \tag{3.20a}$$
$$g_c = \zeta_c \cdot X_{gs} = U_0 k X_{gs} \sin(2kx_s + 2\varphi). \tag{3.20b}$$

As it is convenient for the following calculation, we introduce here parameters ζ_t and ζ_c, which correspond to the change of the frequency of the trapping beam and the control beam due to the particle's position change, respectively. The constant in the expression in the line (3.16e) is $U_0\alpha_t^2 k\sin(2kx_s)+U_0\alpha_c^2 k\sin(2kx_s+2\varphi)=0$, which is guaranteed by the two-field trapping position in equation (3.19).

Taking into consideration these remarks, the dynamical Hamiltonian from the Equation (3.16) becomes:

$$
\begin{aligned}
H_{\mathrm{dyn(amic)}} = &-\hbar\Delta_c(\alpha_c(\hat{a}_c+\hat{a}_c^\dagger)+\hat{a}_c^\dagger\hat{a}_c)+\frac{m\Omega_m^2\hat{x}_m^2}{2}+\frac{p_m^2}{2m} && (3.21a)\\
&-\hbar\zeta_t\alpha_t(\hat{a}_t+\hat{a}_t^\dagger)\hat{x}_m-\hbar\zeta_c\alpha_c(\hat{a}_c+\hat{a}_c^\dagger)\hat{x}_m && (3.21b)\\
&+i\hbar E_t(\hat{a}_t^\dagger e^{-i\phi_t}-\hat{a}_t e^{i\phi_t})+i\hbar E_c(\hat{a}_c^\dagger e^{-i\phi_c}-\hat{a}_c e^{i\phi_c}). && (3.21c)
\end{aligned}
$$

Obtaining the Hamiltonian (3.21) is the first step to the full description of the system. The next step is to express the equations of motion (Langevin equations) of the particle and the light fields from it, which will tell us more about the dynamical behaviour of the system.

3.1.4 Frequency and coupling analysis

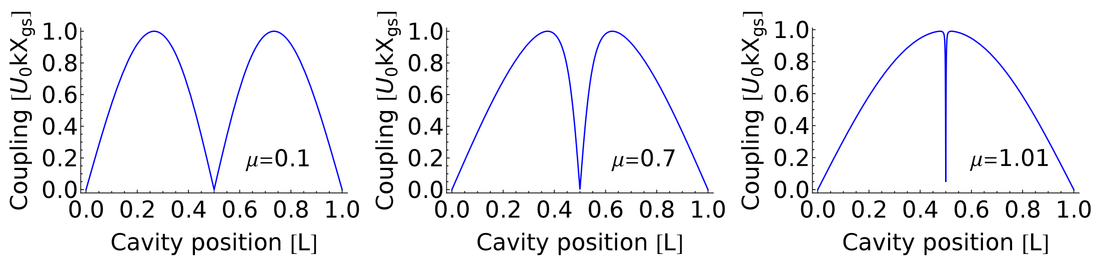

Figure 3.2: **Single-photon coupling for different power ratios μ.** Single-photon coupling of the particle and the control cavity mode, for different power ratios μ. As μ is increased, the point of maximal coupling moves toward the center of the cavity, until $\mu > 1$, when the roles of the two cavity modes are inverted. At the cavity center, the intensity of the control cavity mode is either maximum or 0, therefore the linear coupling at the cavity center is always 0.

Let us shortly focus on the single-photon coupling of the particle to the control cavity field g_c. The trapping position x_s for arbitrary μ can be expressed as $x_s = x_0 + \Delta x$. We have already defined x_0 as the trapping position when $\mu = 0$, while we introduce here Δx as the shift in the trapping position when $\mu \neq 0$. Thus we can eliminate $2kx_0$ from the equation (3.20b) and revise the coupling to:

$$g_c = U_0 k X_{gs} \sin 2(k\Delta x + \varphi). \tag{3.22}$$

As Δx depends on the ratio of powers of the two fields μ (equation (3.19)), the position in the cavity where the coupling is maximal will also depend on μ. We explore this dependence in Figure 3.2, where we plot the coupling as a function of the cavity position, for three distinctly different values $\mu = 0.1$, $\mu = 0.7$ and $\mu = 1.01$. The control field's power is small for $\mu = 0.1$, and therefore its influence on the particle's trapping position is negligible. Therefore, the maximum coupling is reached if the particle is trapped at $L/4$ or $3L/4$, where the control field's intensity changes linearly in the vicinity. The total coupling is the product of the single-photon coupling and the cavity field amplitude α_c (line (3.16d)), which means that it is desired to have higher μ. However, we see that the position of the maximum coupling moves toward the center of the cavity as μ goes closer to 1, which we need to bear in mind when choosing the particle's trapping position. We also notice the ever present dip at the cavity center, where the power of the control field is either zero or maximal, hence no linear coupling is to be expected. When the value of μ goes over 1, the roles of the two fields exchange, and the particle is now predominantly trapped by what we have so far called the control field.

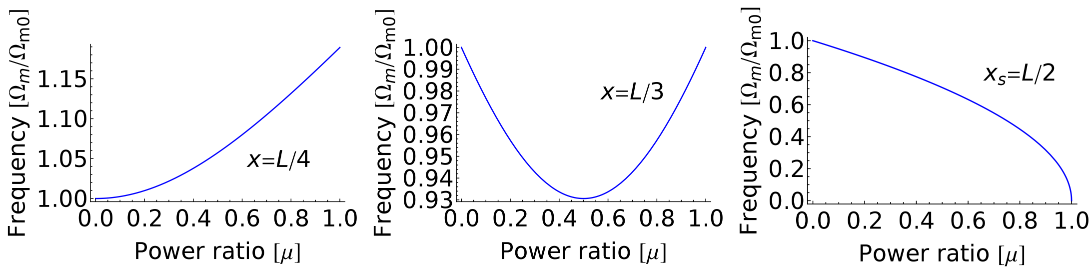

Figure 3.3: **Particle's frequency dependence on the power ratio μ for different trapping positions.** Depending on the trapping position in the cavity, the increase in the power ratio μ differently influences the particle's frequency. When the particle is trapped at $x_s = L/4$, the frequency changes by around 20% when μ goes from 0 to 1. If the particle is trapped at $x_s = L/3$, frequency dependence is symmetric around $\mu = 0.5$. At the cavity center ($x_s = L/2$), the phase between the two field is exactly $\pi/2$, hence the frequency becomes zero when the powers become same and the particle will not be trapped anymore.

We now examine the particle's frequency dependence on μ. By combining equations (3.19) and (3.18), we simplify the expression for Ω_m^2:

$$\Omega_m^2 = \Omega_{m0}^2 \sqrt{1 + \mu^2 + 2\mu \cos 2\varphi}, \tag{3.23}$$

where Ω_{m0}^2 is the particle's oscillating frequency in the absence of the cooling beam:

$$\Omega_{m0}^2 = \frac{2\hbar U_0 k^2}{m}\alpha_t^2. \tag{3.24}$$

We see that the frequency depends only on the ratio of the powers of the optical fields, which we explore in Figure 3.3. We show three distinctive behaviors at three different trapping positions. If the particle is trapped at $x_s = L/4$, the frequency increases with the increasing μ. If $x_s = L/3$, the frequency behavior is symmetric around $\mu = 0.5$. Completely opposite behavior occurs when $x_s = L/2$. The phase φ is equal to $\pi/2$ at this trapping position, thus the control field counteracts the trapping. When $\mu = 1$, we see that $\Omega_m = 0$, which fits with the fact that the two fields cancel each other completely.

3.2 Langevin equations for the system in the cavity

The Hamiltonian of a system, e.g. the Hamiltonian in Equation (3.21), describes the total energy of a system, and is a central starting point in many calculations in quantum mechanics. The time evolution of one of the system variables $A(t)$ is obtained from the equation of motion (Langevin equation) in the interaction picture:

$$\frac{d\hat{A}(t)}{dt} = \frac{i}{\hbar}\left[\hat{H}_{\text{dyn}}, \hat{A}(t)\right]. \tag{3.25}$$

The Langevin equations for the position and the momentum operators of the particle are derived from the Hamiltonian (3.21):

$$\dot{\hat{x}}_m = \frac{\hat{p}_m}{m} \tag{3.26}$$

$$\dot{\hat{p}}_m = -m\Omega_m^2\hat{x}_m - \gamma_m\hat{p}_m + \sum_{j=t,c}\hbar\zeta_j\alpha_j(\hat{a}_j^\dagger + \hat{a}_j) + m\omega_m X_{gs}\eta(t). \tag{3.27}$$

We have introduced two additional terms to equation (3.27), which didn't exist in the Hamiltonian H_{dyn}. Term $-\gamma_m\hat{p}_m$ describes the damping of the particle's motion by the environment, i.e. the gas in the chamber. Collisions between the particle and the gas molecules also act as a random force on the particle, which is represented as $\eta(t)$ in the equation (3.27). This force is described by the correlation property [26]:

$$\langle\eta(t)\eta(t')\rangle = \frac{\gamma_m}{\omega_m}\int\frac{d\omega}{2\pi}e^{-i\omega(t-t')}\omega\coth\left(\frac{\hbar\omega}{2k_BT}\right).$$

The temperature T is the temperature of the motion of the particle. In a temperature range where $k_B T/\hbar \gg \omega_m$, $\coth\left(\frac{\hbar\omega}{2k_B T}\right) \approx \frac{2k_B t}{\hbar\omega}$, such that the correlation becomes delta-correlated:

$$\langle \eta(t)\eta(t')\rangle = \gamma_m \frac{2k_B T}{\hbar\Omega_m}\delta(t-t').$$

Equations of motion (3.26) and (3.27) can be combined to give one second-order differential equation of the motion of the particle:

$$\ddot{\hat{x}}_m + \gamma_m \dot{\hat{x}}_m + \Omega_m^2 \hat{x}_m = \frac{\hbar}{m}\sum_{j=t,c}\zeta_j \alpha_j (\hat{a}_j^\dagger + \hat{a}_j) + \omega_m X_{gs}\eta(t). \tag{3.28}$$

From this equation we can directly read the behaviour of a harmonic oscillator.

By applying the same recipe (equation (3.25)), the Langevin equations for the creation and annihilation operators of the light fields are also recovered from the Hamiltonian (3.21):

$$\dot{\hat{a}}_t = -\kappa(\hat{a}_t + \alpha_t) + E_t e^{-i\phi_t} - \zeta_t \alpha_t \hat{x}_m + \sqrt{2\kappa}(\hat{a}_{c1}^{in} + \hat{a}_{c2}^{in}) \tag{3.29}$$

$$\dot{\hat{a}}_c = -(\kappa + i\Delta_c)(\hat{a}_c + \alpha_c) + E_c e^{-i\phi_c} - \zeta_c \alpha_c \hat{x}_m + \sqrt{2\kappa}(\hat{a}_{t1}^{in} + \hat{a}_{t2}^{in}). \tag{3.30}$$

Equations (3.29) and (3.30) contain the terms which are equivalent to the damping and noise term introduced for the particle's equation of motion (3.27). Damping term $-\kappa(\hat{a}_j + \alpha_j)$ comes from the cavity decay with rate κ, which has already been discussed in (2.20). Cavity linewidth κ, here taken to be equal for both light fields, is equal to the half-width-at-half-maximum of the cavity resonance.

By time-averaging equations (3.29) and (3.30), we find the expression connecting the driving of the cavity E_j and the steady state value α_j:

$$\alpha_t = \frac{E_t e^{-i\phi_t}}{\kappa} \qquad \alpha_c = \frac{E_c e^{-i\phi_c}}{\kappa + i\Delta_c} \tag{3.31}$$

From the combination of equations (3.17) and (3.31), it can be seen that for constant value of μ, desired change of the detuning of the control beam necessitates the change in the driving of the cavity accordingly:

$$\frac{\alpha_c^2}{\alpha_t^2} = \frac{E_c^2}{E_t^2}\frac{\kappa^2}{\kappa^2 + \Delta_c^2} = \mu. \tag{3.32}$$

Another conclusion rising from equation (3.31) is the equality of the phase ϕ_c with the complex phase of the denominator $\kappa + i\Delta_c$. This must be satisfied, as we have already ensured in the previous considerations that α_j and E_j are both real. Hence, ϕ_t needs to be equal to zero, and ϕ_c fulfills:

$$\phi_c = \arccos\frac{\kappa}{\sqrt{\kappa^2 + \Delta_c^2}}. \tag{3.33}$$

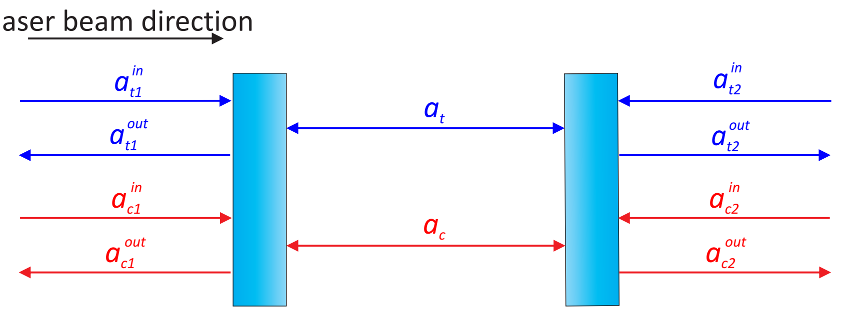

Figure 3.4: **Graphical representation of the input and output fields and the cavity fields.** Two cavity fields, $\hat{a}_t$ (blue) and $\hat{a}_c$ (red), decay with rates $\sqrt{2\kappa}$ into outputs of the two-sided cavity in the system. At the same time, vacuum radiation input noises couple with the same rate to the cavity fields.

Cavity mode amplitudes $\hat{a}_c$ and $\hat{a}_t$ are also influenced by the vacuum radiation input noise, represented in terms $\sqrt{2\kappa}(\hat{a}_{j1}^{in} + \hat{a}_{j2}^{in})$. The two input noises, $\hat{a}_{j1}^{in}$ and $\hat{a}_{j2}^{in}$ correspond to the two sides of the cavity (Figure 3.4). Each noise is coupled to the cavity with a parameter $\sqrt{2\kappa}$ [27]. The correlation functions of the input noises satisfy:

$$\langle \hat{a}_{j1}^{in}(t)\hat{a}_{j1}^{in,\dagger}(t')\rangle = \langle \hat{a}_{j2}^{in}(t)\hat{a}_{j2}^{in,\dagger}(t')\rangle = \delta(t-t') \tag{3.34}$$
$$\langle \hat{a}_{j1}^{in,\dagger}(t)\hat{a}_{j1}^{in}(t')\rangle = \langle \hat{a}_{j2}^{in,\dagger}(t)\hat{a}_{j2}^{in}(t')\rangle = 0. \tag{3.35}$$

Correlation functions of input noises from different cavity inputs and different cavity modes are equal to zero as well.

Equations (3.29) and (3.30) can now be simplified to:

$$\dot{\hat{a}}_c = -(\kappa + i\Delta_c)\hat{a}_c + i\zeta_c\alpha_c\hat{x}_m + \sqrt{2\kappa}(\hat{a}_{c1}^{in} + \hat{a}_{c2}^{in}) \tag{3.36}$$
$$\dot{\hat{a}}_t = -\kappa\hat{a}_t + i\zeta_t\alpha_t\hat{x}_m + \sqrt{2\kappa}(\hat{a}_{t1}^{in} + \hat{a}_{t2}^{in}). \tag{3.37}$$

4 Solving the Langevin equations

Equations (3.26), (3.27), (3.36) and (3.37) form a system of first-order differential equations of motion:

$$\dot{\hat{x}}_m = \frac{\hat{p}_m}{m} \tag{4.1a}$$

$$\dot{\hat{p}}_m = -m\Omega_m^2 \hat{x}_m - \gamma_m \hat{p}_m + \sum_{j=t,c} \hbar\zeta_j \alpha_j (\hat{a}_j^\dagger + \hat{a}_j) + m\Omega_m X_{gs}\eta(t) \tag{4.1b}$$

$$\dot{\hat{a}}_c = -(\kappa + i\Delta_c)\hat{a}_c + i\zeta_c\alpha_c\hat{x}_m + \sqrt{2\kappa}(\hat{a}_{c1}^{in} + \hat{a}_{c2}^{in}) \tag{4.1c}$$

$$\dot{\hat{a}}_t = -\kappa\hat{a}_t + i\zeta_t\alpha_t\hat{x}_m + \sqrt{2\kappa}(\hat{a}_{t1}^{in} + \hat{a}_{t2}^{in}). \tag{4.1d}$$

We solve this system of equations in the Fourier space, a method that has been previously presented in many papers that concern optomechanical systems [19, 26]. However, it is interesting to discuss some steps of the derivation in more detail. Furthermore, we also write some important expressions obtained during the derivation, which will be used in the following chapters.

4.1 Solving by Fourier transformation

We solve the system of equations (4.1) by applying a Fourier transformation (as defined in Appendix 8.A), which creates a set of linear equations out of first-order differential equations:

$$-i\omega\tilde{x}_m(\omega) = \frac{\tilde{p}_m}{m} \tag{4.2a}$$

$$-i\omega\tilde{p}_m(\omega) = -m\Omega_m^2\tilde{x}_m(\omega) - \gamma_m\tilde{p}_m + \sum_{j=t,c}\hbar\zeta_j\alpha_j(\tilde{a}_j^\dagger(-\omega) + \tilde{a}_j(\omega)) + m\Omega_m X_{gs}\tilde{\eta}(\omega) \tag{4.2b}$$

$$-i\omega\tilde{a}_c(\omega) = -(\kappa + i\Delta_c)\tilde{a}_c(\omega) + i\zeta_c\alpha_c\tilde{x}_m(\omega) + \sqrt{2\kappa}(\tilde{a}_{c1}^{in}(\omega) + \tilde{a}_{c2}^{in}(\omega)) \tag{4.2c}$$

$$-i\omega\tilde{a}_t(\omega) = -\kappa\tilde{a}_t(\omega) + i\zeta_t\alpha_t\tilde{x}_m(\omega) + \sqrt{2\kappa}(\tilde{a}_{t1}^{in}(\omega) + \tilde{a}_{t2}^{in}(\omega)). \tag{4.2d}$$

We group $\tilde{a}_j(\omega)$ in equations (4.2c) and (4.2d):

$$\tilde{a}_c(\omega) = \chi_c(\omega)\left(i\zeta_c\alpha_c\tilde{x}_m(\omega) + \sqrt{2\kappa}(\tilde{a}^{in}_{c1}(\omega) + \tilde{a}^{in}_{c2}(\omega))\right) \tag{4.3a}$$

$$\tilde{a}_t(\omega) = \chi_t(\omega)\left(i\zeta_t\alpha_t\tilde{x}_m(\omega) + \sqrt{2\kappa}(\tilde{a}^{in}_{t1}(\omega) + \tilde{a}^{in}_{t2}(\omega))\right), \tag{4.3b}$$

where we have introduced new functions, optical susceptibilities $\chi_c(\omega)$ and $\chi_t(\omega)$:

$$\chi_c(\omega) = \frac{1}{\kappa - i(\omega - \Delta_c)}, \qquad \chi_t(\omega) = \frac{1}{\kappa - i\omega}.$$

We can use equations (4.3) and Hermitian conjugates of these equations, and thus eliminate $\tilde{a}_c(\omega)$ and $\tilde{a}_t(\omega)$ from equation (4.2b). We first express $\tilde{a}_j(\omega) + \tilde{a}^\dagger(-\omega)$:

$$\tilde{a}_c(\omega) + \tilde{a}^\dagger_c(-\omega) = (\chi_c(\omega) - \chi^*_c(-\omega))\, i\zeta_c\alpha_c\tilde{x}_m(\omega) + O(\omega) \tag{4.4a}$$

$$\tilde{a}_t(\omega) + \tilde{a}^\dagger_t(-\omega) = (\chi_t(\omega) - \chi^*_t(-\omega))\, i\zeta_t\alpha_t\tilde{x}_m(\omega) + M(\omega). \tag{4.4b}$$

However, $\chi_t(\omega) = \chi^*_t(-\omega)$, so $\tilde{a}_t(\omega) + \tilde{a}^\dagger_t(-\omega) = M(\omega)$. For conciseness, we use functions $O(\omega)$ and $M(\omega)$, which contain the vacuum radiation input noises:

$$\begin{aligned} O(\omega) &= \sqrt{2\kappa}\left[\chi_c(\omega)(\tilde{a}^{in}_{c1}(\omega) + \tilde{a}^{in}_{c2}(\omega)) + \chi^*_c(-\omega)(\tilde{a}^{in,\dagger}_{c1}(-\omega) + \tilde{a}^{in,\dagger}_{c2}(-\omega))\right] \\ M(\omega) &= \sqrt{2\kappa}\chi_t(\omega)\left[\tilde{a}^{in}_{t1}(\omega) + \tilde{a}^{in}_{t2}(\omega) + \tilde{a}^{in,\dagger}_{t1}(-\omega) + \tilde{a}^{in,\dagger}_{t2}(-\omega)\right]. \end{aligned}$$

Equations (4.4) and (4.2a) can be used to eliminate $\tilde{a}_c(\omega)$, $\tilde{a}_t(\omega)$ and $\tilde{p}_m(\omega)$ from equation (4.2b):

$$\begin{aligned} m\tilde{x}_m(\omega)\left(\Omega_m^2 - \omega^2 - i\gamma_m\omega + 2\frac{g_c^2\alpha_c^2\Delta_c\Omega_m(\kappa^2 - \omega^2 + \Delta^2 + 2i\kappa\omega)}{(\kappa^2 + (\omega + \Delta_c)^2)(\kappa^2 + (\omega - \Delta_c)^2)}\right) &= \\ m\Omega_m X_{gs}\tilde{\eta}(\omega) + \hbar\zeta_c\alpha_c O(\omega) + \hbar\zeta_t\alpha_t M(\omega). \end{aligned} \tag{4.5}$$

Spotting the similarity to equation (2.6), we define the effective mechanical susceptibility of the particle's oscillation to be:

$$\chi_m^{\text{eff}}(\omega) = \frac{\Omega_m}{\Omega_m^2 - \omega^2 - i\gamma_m\omega + 2\frac{g_c^2\alpha_c^2\Delta_c\Omega_m(\kappa^2 - \omega^2 + \Delta^2 + 2i\kappa\omega)}{(\kappa^2 + (\omega + \Delta_c)^2)(\kappa^2 + (\omega - \Delta_c)^2)}}.$$

In comparison to the susceptibility defined for the classical harmonic oscillator in equation (2.7), susceptibility $\chi_m^{\text{eff}}(\omega)$ has an additional part due to the interaction with the (detuned) light field in the cavity. However, we can introduce the effective oscillator's frequency ω_m^{eff} and damping γ_m^{eff} as:

$$\Omega_m^{\text{eff}}(\omega) = \left[\Omega_m^2 + \frac{2g_c^2|\alpha_c|^2\Omega_m\Delta_c\left[\kappa^2 - \omega^2 + \Delta_c^2\right]}{(\kappa^2 + (\omega + \Delta_c)^2)\left(\kappa^2 + (\omega - \Delta_c)^2\right)}\right]^{1/2} \tag{4.6a}$$

$$\gamma_m^{\text{eff}}(\omega) = \gamma_m - \frac{4g_c^2|\alpha_c|^2\Omega_m\Delta_c\kappa}{(\kappa^2 + (\omega + \Delta_c)^2)\left(\kappa^2 + (\omega - \Delta_c)^2\right)}. \tag{4.6b}$$

Functions $\omega_m^{\text{eff}}(\omega)$ and $\gamma_m^{\text{eff}}(\omega)$ depend on the spectral frequency ω, which is a product of Fourier transform. Therefore, the frequency ω at which these functions are evaluated isn't properly defined. This difficulty can be circumvented as in [26], where it has been assumed that both functions don't change considerably with changing frequency ω. However, one needs to use this trick with great care, as the damping could increase to a significant value. Still, we can use them to express $\chi_m^{\text{eff}}(\omega)$ in a more compact way:

$$\chi_m^{\text{eff}}(\omega) = \frac{\Omega_m}{\left(\Omega_m^{\text{eff}}(\omega)\right)^2 - \omega^2 - i\gamma_m^{\text{eff}}(\omega)\omega}.$$

4.2 Noise power spectrum of particle's motion

As we have seen in equation (4.5), the Fourier transform of the particle's motion $\hat{x}_m$ is:

$$\tilde{x}_m(\omega) = \chi_m^{\text{eff}}(\omega)X_{gs}\tilde{\eta}(\omega) + \chi_m^{\text{eff}}(\omega)X_{gs}g_c\alpha_c O(\omega) + \chi_m^{\text{eff}}(\omega)X_{gs}g_t\alpha_t M(\omega).$$

The noise power spectrum (NPS) of $\hat{x}_m$ can be directly obtained from $\tilde{x}_m(\omega)$ (Appendix 8.A):

$$\langle\tilde{x}_m(\omega)\tilde{x}_m(\omega')\rangle = S_{xx}(\omega)\delta(\omega+\omega') = \left|\chi_m^{\text{eff}}(\omega)\right|^2 [S_{\text{th}}(\omega) + S_{\text{rp}}(\omega)]\delta(\omega+\omega'), \tag{4.7}$$

where $S_{\text{rp}}(\omega)$ is the radiation pressure contribution and $S_{\text{th}}(\omega)$ is the thermal noise contribution with:

$$S_{\text{th}}(\omega) = X_{gs}^2\tilde{\eta}(\omega)\tilde{\eta}^\dagger(-\omega) = X_{gs}^2\gamma_m\frac{2k_BT}{\hbar\Omega_m}.$$

The expression for $S_{\text{rp}}(\omega)$ is not the part of this study, and we restrict ourselves only to the thermal contribution. The NPS of particle's motion is then:

$$S_{xx}(\omega) = X_{gs}^2\frac{\gamma_m\Omega_m^2}{\left(\left(\Omega_m^{\text{eff}}(\omega)\right)^2 - \omega^2\right)^2 + \left(\gamma_m^{\text{eff}}(\omega)\omega\right)^2}\frac{2k_BT}{\hbar\Omega_m}, \tag{4.8}$$

which reminds us of the expression for the classical harmonic oscillator. If we use $X_{gs}^2 = \frac{\hbar}{m\Omega_m}$, we can further simplify equation (4.8):

$$S_{xx}(\omega) = \frac{2k_BT}{m}\frac{\gamma_m}{\left(\left(\Omega_m^{\text{eff}}(\omega)\right)^2 - \omega^2\right)^2 + \left(\gamma_m^{\text{eff}}(\omega)\omega\right)^2}. \tag{4.9}$$

5 Experimental detection of the particle's motion

We have shown in equations (4.6) that the control field changes both the particle's frequency and the damping that it experiences. However, we can also employ the coupling between the control field and the particle's motion in order to monitor the particle's motion (equation (4.3a)). We present here a detection method which exploits this coupling, split into an optical and an electronic part. We also introduce the theoretical model of detection, where we show the connection between the detected noise power spectrum, which is effectively a NPS of optical quadratures of a cavity field, and the genuine noise power spectrum of the particle's motion.

5.1 Optical path

The first part of the detection scheme, the optical path, is shown in Figure 5.1. Note that we first present the detection in time domain, but with the frequencies of the light field set such that we are in a frame rotating at the control field frequency. Therefore, the trapping beam has the frequency $\delta\omega = \omega_c - \omega_t$ in that frame.

The control cavity field leaks out of the cavity with a rate of $\sqrt{2\kappa}$. The output of the cavity is related to the cavity field by the cavity input-output relation [27]:

$$\hat{a}_{c2}^{out}(t) = \sqrt{2\kappa}\hat{a}_c(t) - \hat{a}_{c2}^{in}(t), \tag{5.1}$$

where $\hat{a}_{c2}^{in}$ describes the vacuum radiation input noise at the cavity back mirror (i.e., the side from which the cavity is not driven). We concentrate only on the leaking cavity field, i.e. we don't explore the influence of the input noise $\hat{a}_{c2}^{in}(t)$ to the output light field in the further text. This input noise is not dependent on the system in the cavity, hence it will always be present in the detected noise power spectrum.

Note that the trapping cavity field also leaks out of the cavity. In order to separate it from the optical path of the control field, we use the fact that the two beams are orthogonally polarized, which means that they can be separated on a polarizing beamsplitter (PBS1). Quarter-wave plate QWP1 and half-wave plate HWP1 in front of PBS1 set the linear polarizations of the trapping and the control beam to vertical and horizontal, respectively. Therefore, the trapping beam is reflected at PBS1, while the control beam is transmitted. The power of the trapping beam is monitored in the reflected arm at the detector DET1 (custom-built detector).

The control beam is then spatially overlapped at the beamsplitter PBS2 with a strong, vertically polarized local oscillator (LO). The LO is taken from the trapping beam before the cavity and, as such, has the same frequency $\delta\omega = FSR + \Delta$ as the trapping beam. The amplitude of the LO field can be written as:

$$\hat{a}_{LO}(t) = \alpha_{LO} \cdot e^{-i(\delta\omega t + \phi_{\mathrm{opt}})}, \tag{5.2}$$

where ϕ_{opt} is the phase of the LO. In the experiment, the power of the LO is set to be around 10 times bigger than the power of the control beam, hence α_{LO} can be assumed to be real.

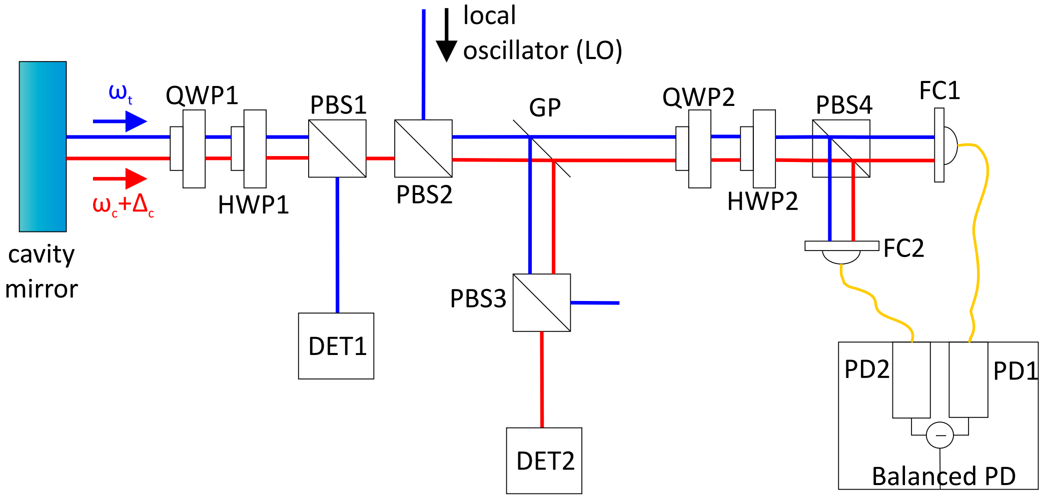

Figure 5.1: **Optical path after the cavity.** The trapping beam is separated from the control beam on a polarizing beamsplitter (PBS1) and detected using a detector (DET1). We use a quarter-wave plate (QWP1) and a half-wave plate (HWP1) to ensure that the polarizations are set properly. The local oscillator (LO) is spatially overlapped with the control beam on a separate beamsplitter (PBS2). Glass plate (GP) reflects around 4% of both beams. In the reflected arm, the LO is separated from the control beam on the PBS3 and the control beam is detected on a detector (DET2). The polarization of light transmitted through GP is rotated by 45° using QWP2 and HWP2. Light is then split into two parts on $PBS4$, collected by fiber couplers FC1 and FC2 and used in balanced photodetection (PD1 and PD2) to amplify the control beam amplitude.

As it influences the particle's frequency and damping, it is necessary to control the ratio of the powers of the two beams μ, given in equation (3.17). We have already mentioned that we monitor the power of the trapping beam at DET1. We use a glass plate (GP) to split some control field after the PBS2, in order to measure its power. The glass plate GP reflects around 4% of both LO and the control beams. The LO is vertically polarized and can be separated from the control beam with the beamsplitter PBS3. The remaining light, which is a small part of the control beam leaking from the cavity, is detected on the detector DET2 (InGaAs Avalanche Photodetector APD110C, Thorlabs). The ratio of the measured powers from DET2 and DET1 is calibrated to show the ratio of the powers at the output of the cavity, which corresponds to the value of μ. We keep μ stable by regulating the intensity of the control beam.

The light transmitted through the glass plate comes to the balanced detection part of the scheme. The polarizations of both beams are rotated with QWP2 and HWP2 by 45°. This creates the following superpositions of light fields in different outputs of the PBS4:

$$\begin{aligned} \text{to PD1} : \hat{d}_1(t) &= \frac{1}{\sqrt{2}}(\hat{a}_{c2}^{out}(t) + \hat{a}_{LO}(t)) \\ \text{to PD2} : \hat{d}_2(t) &= \frac{1}{\sqrt{2}}(\hat{a}_{c2}^{out}(t) - \hat{a}_{LO}(t)). \end{aligned}$$

Detectors PD1 and PD2 measure the powers, which are proportional to $|\hat{d}_1(t)|^2$ and $|\hat{d}_2(t)|^2$, respectively. The balanced photodetector takes the difference of measured values:

$$\begin{aligned} l(t) &= \frac{1}{2}\left(|\hat{a}_{c2}^{out} + \hat{a}_{LO}|^2 - |\hat{a}_{c2}^{out} - \hat{a}_{LO}|^2\right) = \hat{a}_{c2}^{out}\hat{a}_{LO}^* + \hat{a}_{c2}^{out\dagger}\hat{a}_{LO} \\ &= \hat{a}_{c2}^{out}\alpha_{LO}^* \cdot e^{i(\delta\omega t + \phi_{\text{opt}})} + \hat{a}_{c2}^{out\dagger}\alpha_{LO} \cdot e^{-i(\delta\omega t + \phi_{\text{opt}})}. \end{aligned} \tag{5.3}$$

Hence, $l(t)$ contains a beat signal at frequency $\delta\omega$ with sidebands, created due to the modulation introduced by the particle motion.

5.2 Electronic path

We proceed with the electronic part of the detection setup, which is used to demodulate the detected signal $l(t)$. The brief sketch can be seen in Figure 5.2.

The balanced photodetector outputs an electronic signal $l(t)$ (equation (5.3)) with a carrier frequency $\delta\omega$ and the sidebands from the particle's motion with frequencies $\delta\omega - \Omega_m$ and $\delta\omega + \Omega_m$. This signal is then demodulated by mixing (multiplication) with an electronic local oscillator (ELO), created by a signal generator and with the same frequency:

$$l_{ELO}(t) \propto \sin(\delta\omega t + \phi_{\mathrm{ELO}}),$$

where ϕ_{ELO} is the relative electronic phase between the signal $l(t)$ and the electronic local oscillator. We detect only the slowly oscillating terms on the spectrum analyzer and therefore omit the high frequency terms around $2\delta\omega$. The resulting signal is (up to a proportionality factor):

$$s_{\mathrm{opt}}(t) = \hat{a}_{c2}^{out} e^{i\theta} + \hat{a}_{c2}^{out,\dagger} e^{-i\theta}. \tag{5.4}$$

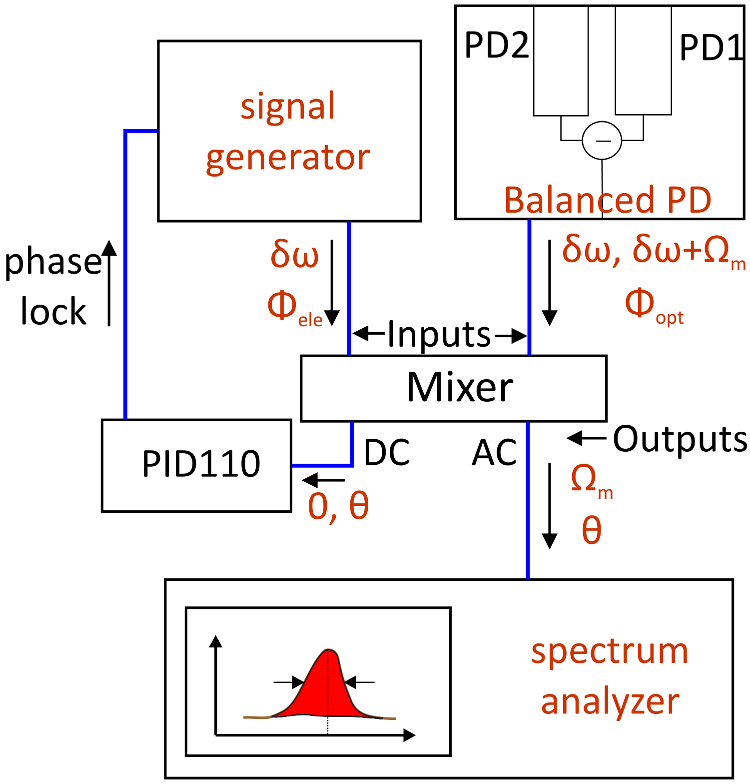

Figure 5.2: **Electronic path in the detection scheme.** Detected signal with a carrier frequency $\delta\omega$ and phase ϕ_{opt} and with sidebands at the particle's frequency Ω_m, is multiplied on a mixer with a sine signal created by a signal generator, which has the frequency $\delta\omega$ and phase ϕ_{ele}. The DC part of the product is fed to the proportional differential regulator (PID 110, Toptica), which is used to stabilize the overall phase $\theta = \phi_{\mathrm{ELO}} + \phi_{\mathrm{opt}} = \pi/2$. The AC part of the demodulated signal, now with the main frequency Ω_m, is fed to the spectrum analyzer, which shows its noise power spectrum.

This exactly corresponds to the signal one would obtain directly by balanced homodyne detection of the control beam with an optical local oscillator of the same frequency. This method, which uses an intermediate frequency as a carrier of the signal, is being use in radio technology and is called the superheterodyne detection [28]. The phase $\theta = \phi_{\text{ELO}} + \phi_{\text{opt}}$ determines the detected quadrature of the control beam. In order to extract the phase modulation of the control beam, we experimentally set $\theta = \pi/2$ via the electronic phase ϕ_{ELO}, thereby compensating for the optical phase ϕ_{opt} in the setup:

$$s_{\text{opt}}(t) = i(\hat{a}_{c2}^{out} - \hat{a}_{c2}^{out,\dagger}) \tag{5.5}$$

The phase θ is kept stable by using a proportional differential regulator, which communicates back with the signal generator in order to change ϕ_{ELO}.

The Fourier transform $\tilde{s}_{\text{opt}}(\omega)$ is then easily obtained:

$$\tilde{s}_{\text{opt}}(\omega) = i(\tilde{a}_{c2}^{out}(\omega) - \tilde{a}_{c2}^{out,\dagger}(\omega)) \tag{5.6}$$

The noise power spectrum of the signal $s_{\text{opt}}(t)$ is obtained by calculating the $S_{\frac{\pi}{2}\frac{\pi}{2}}(\omega) = \langle \tilde{s}_{\text{opt}}(\omega)\tilde{s}^{\dagger}_{\text{opt}}(\omega)\rangle$:

$$S_{\frac{\pi}{2}\frac{\pi}{2}}(\omega') = 2\kappa\zeta_c^2\alpha_c^2 \left|\chi_c(\omega) + \chi_c^*(-\omega)\right|^2 S_{xx}(\omega)\delta(\omega - \omega'). \tag{5.7}$$

In the experiment, the signal $s_{\text{opt}}(t)$ is fed to the spectrum analyzer, which outputs its spectrum. Up to a proportionality factor, Equation 5.7 resembles the result of the detection described in [29], and allows us to derive the mechanical NPS $S_{xx}(\omega)$ from the detected signal.

6 Evaluation of experimental data

In the experiment, we measure the noise power spectrum for changing ratio of the powers μ and detuning of the control beam Δ_c. As we have shown in equation (5.7), the measured NPS is related to the particle's NPS with a proportionality function, which is frequency-dependent. We firstly demonstrate here the procedure for extracting the particle's NPS from the measured NPS. Once we obtain the particle's NPS, we show the fitting of the harmonic oscillator spectrum. We then proceed by testing the theoretical model dependencies from the fitted particle's frequency and damping.

6.1 Extraction of particle's noise power spectrum

We have derived a theoretical expression for the NPS of the particle's motion $S_{\frac{\pi}{2}\frac{\pi}{2}}(\omega)$ in equation (5.7). However, the actual system has electronic and optical noise which were unaccounted for in the theoretical model. We haven't included any treatment of classical laser intensity and phase noise in our study, which could have implications on the particle's NPS through optomechanical coupling [30]. The overall electronic noise can be measured separately and subsequently extracted from the measured NPS. Instead, we rely on measuring the NPS of the background noise when there are no trapped particles in the cavity, and accordingly subtracting it from the measured NPS with the particle's motion. We check this on the experimental NPS for three different control beam detunings $\Delta_c^a = 0$ kHz, $\Delta_c^b = 128.7$ kHz and $\Delta_c^c = 207.9$ kHz (Figure 6.1). The ratio between the powers of the control and the trapping beam is for all graphs $\mu = 0.3$. The left column shows overlapped NPS with a particle's oscillation NPS (blue trace) and without it (red trace), while the second column shows the difference of the two NPS. We note that the subtracted NPS has a ground level at $0\,\mathrm{V^2/Hz}$, just as expected if all the constant noise sources have been eliminated.

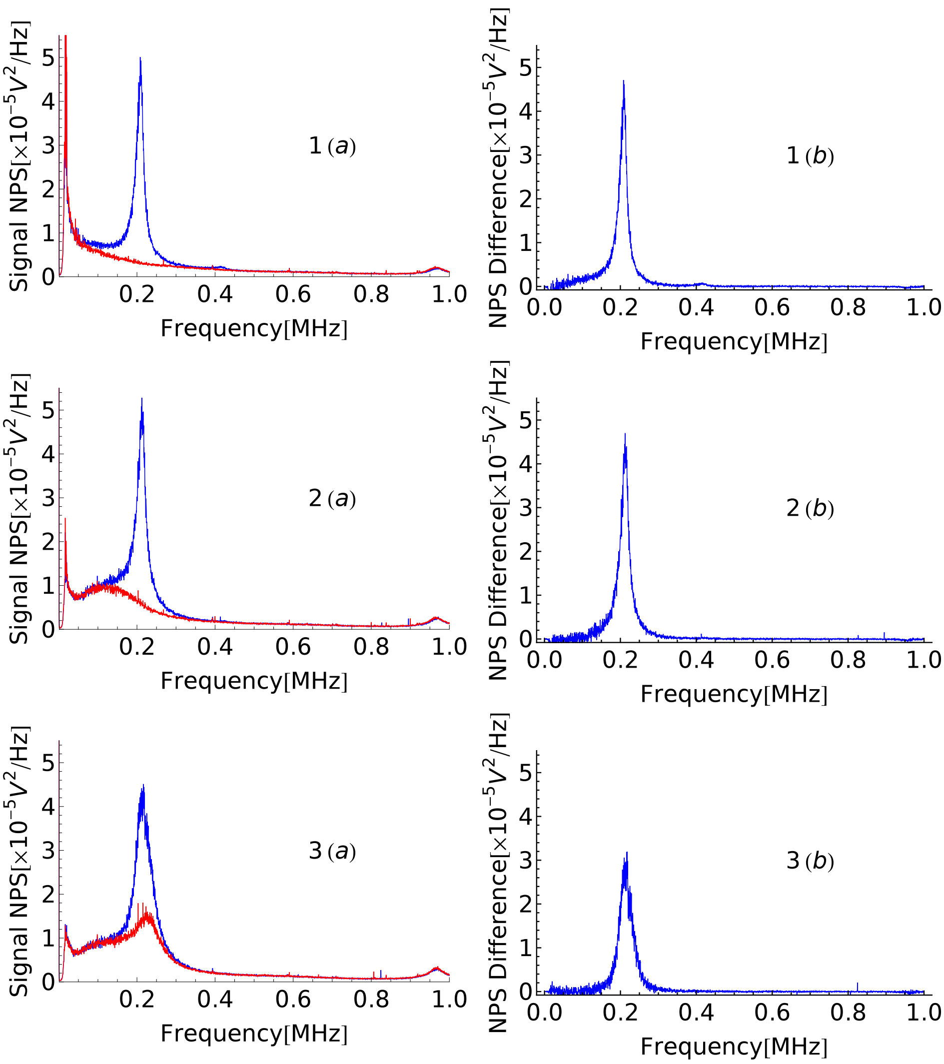

Figure 6.1: **Subtraction of background spectrum from the spectrum with a particle.** Column (a) shows the comparison of the NPS of the signal with the particle's NPS (blue) and without it (red) for three different detuning frequencies of the control field: 1. $\Delta_c = 0$ kHz, 2. $\Delta_c = 128.7$ kHz and 3. $\Delta_c = 207.9$ kHz. Some noise peaks can be seen in both NPS, which disappear in their difference, shown in column (b). The power ratio is $\mu = 0.3$ in all graphs.

To reconstruct the NPS of the particle S_{xx}, we need to account for the frequency-dependent filtering by the cavity, which also depends on the detuning Δ_c. We therefore divide $S_{\frac{\pi}{2}\frac{\pi}{2}}(\omega)$ by $\kappa|\chi_c(\omega) + \chi_c^*(-\omega)|^2$, following equation (5.7). The cavity amplitude HWHM κ has been measured independently to be $\kappa = (40 \pm 3)$ kHz by observing the cavity transmission. The comparison of the NPS before and after the division is shown in Figure 6.2, for the same three detuning frequencies as before. We see that the noise at higher frequencies increases after the division, which is expected as $|\chi_c(\omega) + \chi_c^*(-\omega)|^2$ decreases fast with increasing ω. The size of the peak of the particle's NPS looks about the same for $\Delta_c = 0$ and $\Delta_c = 128.7$ kHz, while after dividing the spectra, the peak size at $\Delta_c = 0$ is clearly larger. As the peak size is proportional to the temperature of particle's motion, we expect to cool the particle's motion when we increase the detuning until this has the maximum effect around $\Delta_c \approx \Omega_m$.

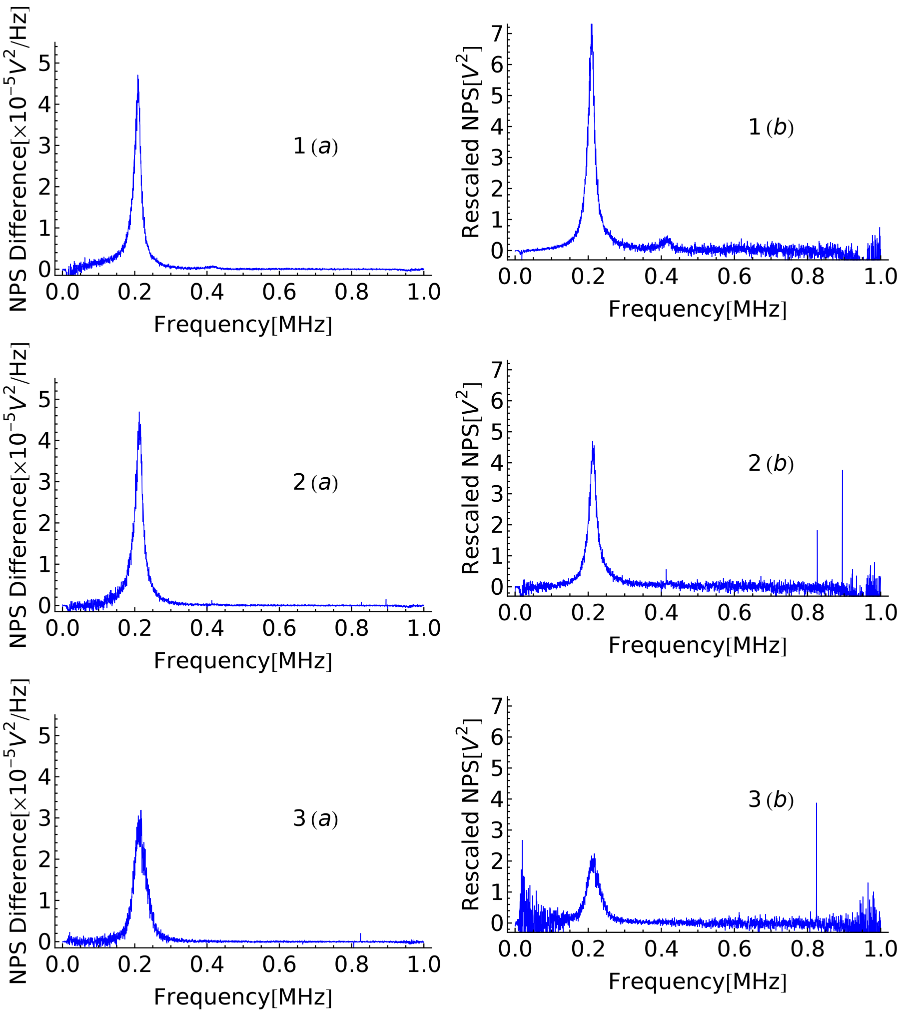

Figure 6.2: **Dividing the spectra by** $\kappa|\chi_c(\omega) + \chi_c^*(-\omega)|^2$**.** On the left side (spectra (a)) the NPS obtained by previous subtraction are shown, while on the right (column (b)) the spectra divided by the cavity filter function can be seen. Three sets of spectra have three different detunings of the control field: 1. $\Delta_c = 0$ kHz, 2. $\Delta_c = 128.7$ kHz and 3. $\Delta_c = 207.9$ kHz.

By dividing the measured NPS by the cavity filter function, we have obtained the NPS which corresponds to the spectrum of particle's motion S_{xx} (equation (4.9)) multiplied by a detuning-independent constant, which still contains the coupling. We can determine the effective frequency Ω_m^{fit} and damping γ_m^{fit} by fitting the harmonic oscillator spectrum:

$$S_{xx}^{\text{fit}}(\omega) = \frac{a^{\text{fit}}}{2\pi} \frac{\gamma_m}{(\omega^2 - \Omega_m^{\text{fit}})^2 + (\gamma_m^{\text{fit}}\omega)^2}. \tag{6.1}$$

We also obtain the multiplicative constant a^{fit}, which depends on coupling and the temperature of the particle's motion. The example of fits done on NPS in the column (b) of Figure 6.2 are shown in Figure 6.3, while the fit parameters are shown in Table 6.1. In general, we see that the fits follow the NPS quite well, which we can also put to a test by plotting the fit parameters with respect to the detuning or power ratio, which we set to do in the following text. In order to do so, we fit NPS for a wide range of power ratios μ and detunings Δ_c.

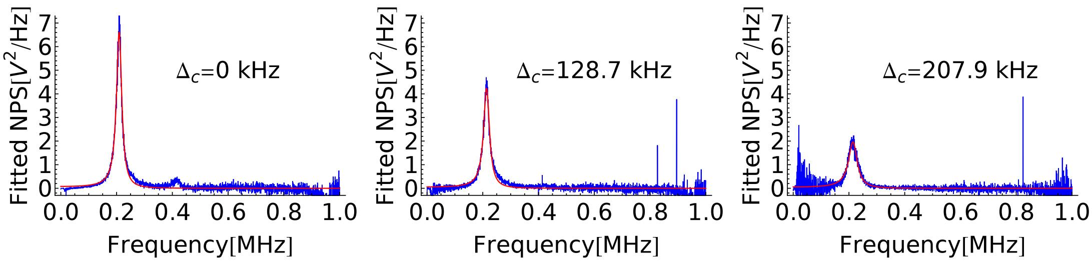

Figure 6.3: **Fitted particle's NPS.** We fit the processed measured NPS (blue trace) with a theoretical dependence S_{xx} and extract the frequency, width and area of the peak. The fits (red line) follow the experimental data well.

Δ_c [kHz]	γ_m^{fit} [kHz]	ω_m^{fit}[kHz]	a^{fit}[a.u.]
0	23.1	209.8	42.0
128.7	25.7	214.4	31.4
207.9	37.7	216.0	21.6

Table 6.1: Fit parameters γ_m^{fit}, Ω_m^{fit} and a^{fit} for three different detunings $\Delta_c = 0$ kHz, $\Delta_c = 128.7$ kHz and $\Delta_c = 207.9$ kHz.

6.2 Particle frequency and trapping position

We have already shown in equation (3.23) that the particle's frequency Ω_m depends on the ratio of powers μ. For a constant trapping power, we change μ in the experiment, set the detuning $\Delta_c = 0$ kHz and measure the NPS. We evaluate the NPS as explained in the previous text to obtain the particle's frequency. Figure 6.4 shows the dependence of the frequency on the power ratio (blue points), which we then fit by the theoretical dependence (red line). The fit parameters are the particle's trapping position $x_s^{\rm fit} = (1.54 \pm 0.02)$ mm and the particle's unmodified frequency at $\mu = 0$ $\Omega_{m0} = (228.8 \pm 0.5)$ kHz. We also evaluate the trapping position independently from a picture of a trapped particle in the cavity taken by a camera (See Appendix 8.D for details), which gives $x_s^{\rm camera} = (1.38 \pm 0.07)$ mm. If we compare $x_s^{\rm fit}$ and $x_s^{\rm camera}$, we see that the two values are reasonably close to each other.

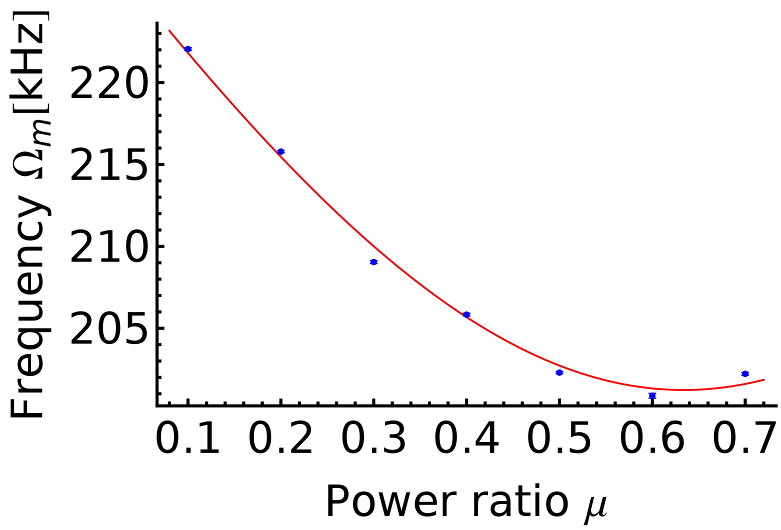

Figure 6.4: **Particle's frequency Ω_m vs. ratio of powers μ.** Particle's frequency, evaluated from the fit of the particle's NPS, is shown here together with error bars versus the ratio of powers μ. We fit the theoretical dependence from equation (3.23), which we use to extract the trapping position of the particle $x_s^{\rm fit} = (1.54 \pm 0.02)$ mm. We also obtain the particle's frequency at $\mu = 0$: $\Omega_{m0} = (228.8 \pm 0.5)$ kHz.

6.3 Effective particle frequency and damping

In equations (4.6), we have introduced the particle's effective frequency $\Omega_m^{\rm eff}(\omega)$ and damping $\gamma_m^{\rm eff}(\omega)$. Both variables depend on the spectral frequency ω, thus it is not straightforward to examine the dependence on the detuning Δ_c. However, we follow the logic set in [26], where the frequency and damping are evaluated at the original frequency Ω_m. We set the power ratio $\mu = 0.3$, and measure the NPS for different detuning frequencies Δ_c in the range $[0\ \text{kHz}, 350\ \text{kHz}]$. By fitting the measured NPS, we obtain a set of fit parameters corresponding to the particle's frequency and damping. We fit functions $\Omega_m^{\text{eff}}(\Omega_m)$ and $\gamma_m^{\text{eff}}(\Omega_m)$ to the experimentally obtained values, which we show in Figure 6.5. The fit of the effective frequency recovers the behavior similar to the plot of experimental data points, but there is still some discrepancy. This is most obviously seen at 0 kHz, where we expect the fit to contain the value of frequency. Contrary to this fit, the fit of the effective damping follows the experimental data more closely. A proper fitting procedure has since been suggested in [20].

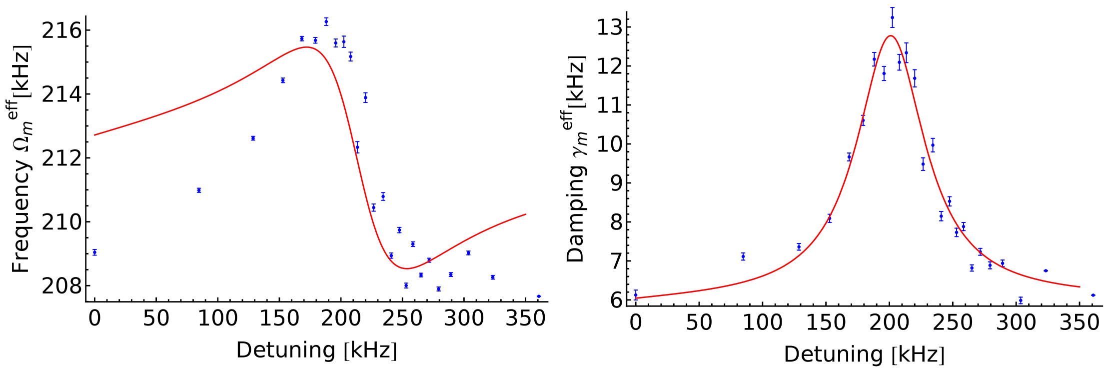

Figure 6.5: **Effective frequency Ω_m^{eff} and damping γ_m^{eff} versus detuning Δ_c.** We fit the dependence of the effective frequency Ω_m^{eff} and damping γ_m^{eff} on the control field detuning Δ_c. We use the functions from the theoretical model, which we evaluate at the frequency $\omega = \Omega_m$.

Both fits give as fit parameters the cavity decay rate κ, the particle's frequency Ω_m at $\Delta_c = 0$ kHz and the coupling constant g_c, while the effective damping fit also provides the value for the elementary damping γ_m. These parameters are compared in Table 6.2, which shows that the fit parameters are of the similar size. The cavity amplitude HWHM κ fits well to the independently measured value $\kappa = (40 \pm 3)$ kHz.

Fit parameter	From the fit of Ω_m^{eff}	From the fit of γ_m^{eff}
κ[kHz]	42 ± 12	33 ± 3
Ω_m[kHz]	212.7 ± 0.4	201 ± 2
g_c [kHz]	24 ± 4	14.9 ± 0.8
γ_m [kHz]	-	6.0 ± 0.3

Table 6.2: Fit parameters κ, Ω_m, g_c and γ_m from the fits of the effective frequency and damping.

7 Conclusion and outlook

We have presented a full theoretical model for a dielectric sub-micron particle interacting with two optical cavity mode fields through the dipole interaction. In parallel to the theoretical model, we have described an experiment designed to explore this interaction. We particularly focused on the experimental detection setup, which was devised in order to extract the particle's motion from the noise power spectrum of one of the optical fields. We demonstrated the process of the extraction of the NPS of the particle's motion from the detected spectrum, where we have first subtracted the everpresent noise background, followed by dividing the NPS by a cavity filter function. We then show that the theoretical expression for the harmonic oscillator fits the extracted spectrum well, with the particle's frequency, damping and a constant proportional to the temperature of motion being the fit parameters.

One of the open questions is the influence of laser classical intensity and phase noises, which has been considered in [31]. Also, we haven't explored the influence of shot noises on the particle's NPS, which are contained in the radiation pressure contribution. We hope to address these questions in the following studies.

We have shown the theoretical dependence of the particle's frequency on the ratio of the powers of the two optical fields, as well as the particle's trapping position in the cavity. We fitted the experimental dependence on the power ratio, which we used to determine the trapping position. The trapping position fits within 10% of the value determined from a picture of the trapped particle in the cavity.

We have also explored the theoretical dependence of the single-photon coupling to the control field versus the power ratio. For small power ratio, we don't expect that the particle's trapping position changes a lot. Therefore, the position where the particle experiences the maximum coupling is at 1/4 and 3/4 of the cavity length. However, a stronger control beam will influence the trapping position, and the position of the maximum coupling would move toward the cavity center. The particle's total coupling depends on the control electric field's amplitude and therefore stronger optomechanical effects could be reached in the region of higher power ratio, closer to the cavity center.

8 Appendices

Appendix 8.A Fourier transform notation

We will summarize the properties of the Fourier transform in the following text. We follow the definition of the Fourier transform $\mathcal{F}$, as used in [32]:

$$\mathcal{F}(\hat{f}(t)) = \tilde{f}(\omega) = \int\limits_{-\infty}^{+\infty} dt\, \hat{f}(t) e^{i\omega t}.$$

It can be shown that this implies that the Fourier transform of the Hermitian conjugate of the operator f is then:

$$\mathcal{F}(\hat{f}^{\dagger}(t)) = \tilde{f}^{\dagger}(\omega) = \left(\tilde{f}(-\omega)\right)^{\dagger},$$

which, by convention, we write just as $\tilde{f}^{\dagger}(-\omega)$. The inverse Fourier transform has an additional factor of 2π:

$$\hat{f}(t) = \mathcal{F}(\tilde{f}(\omega)) = \frac{1}{2\pi} \int\limits_{-\infty}^{+\infty} d\omega\, \tilde{f}(\omega) e^{-i\omega t}$$

The Fourier transform of the arbitrary n-th order time-derivative $\frac{d^n}{dt^n}\hat{f}(t)$ is transformed as:

$$\mathcal{F}\left(\frac{d^n}{dt^n}\hat{f}(t)\right) = (-i\omega)^n \tilde{f}(\omega).$$

Fourier transform $\tilde{f}(\omega)$ doesn't have any physical meaning. However, its moments have physical meaning [33]:

$$\langle \tilde{f}(\omega_1)\tilde{f}^{\dagger}(-\omega_2)\rangle = \tilde{f}(\omega_1)\tilde{f}^{\dagger}(-\omega_1)\delta(\omega_1 - \omega_2) = S(\omega_1)\delta(\omega_1 - \omega_2), \qquad (8.1)$$

where $S(\omega_1)$ is the spectrum of signal $f(t)$.

Appendix 8.B Polarizability of a spherical particle

The problem of a dielectric sphere in an uniform electric field is a known problem in electrostatics. We follow the derivation of the polarizability of the sphere as provided in [34] and give a brief sketch of the derivation.

We assume the uniform electric field is propagating along the z axis in the environment with a dielectric constant ε_2 and has amplitude E_0. The sphere of radius R and dielectric constant ε_1 is put in this field. We need to solve the Laplace equation for the inside of the sphere and the outside, with boundary conditions set at $r = R$ and $r \to \infty$. The solutions of the Laplace equation are:

$$\Phi_{\text{in}} = \sum_{l=0}^{\infty} A_l r^l P_l(\cos\theta), \tag{8.2a}$$

$$\Phi_{\text{out}} = \sum_{l=0}^{\infty} \left[B_l r^l + C_l r^{-(l+1)}\right] P_l(\cos\theta). \tag{8.2b}$$

The boundary condition at $r \to \infty$ ($\Phi \to -E_0 r\cos\theta$) sets that $B_1 = -E_0$ and $B_{l\neq 1} = 0$. The boundary condition at the surface of the sphere ($r = R$) postulates the continuity of the tangential electric field $-\frac{1}{R}\frac{\partial\Phi}{\partial\theta}$ and the normal electric displacement field $-\varepsilon\frac{\partial\Phi}{\partial r}$, which determines the constants A_l and C_l:

$$A_1 = -\left(\frac{3\varepsilon_2}{2\varepsilon_2 + \varepsilon_1}\right) E_0, \quad A_{l\neq 1} = 0 \tag{8.3a}$$

$$C_1 = -\left(\frac{\varepsilon_1 - \varepsilon_2}{2\varepsilon_2 + \varepsilon_1}\right) R^3 E_0, \quad C_{l\neq 1} = 0. \tag{8.3b}$$

Outside the sphere, the potential then has the shape:

$$\Phi_{\text{out}} = -E_0 r\cos\theta + \left(\frac{\varepsilon_1 - \varepsilon_2}{\varepsilon_1 + 2\varepsilon_2}\right) E_0 \frac{R^3}{r^2}\cos\theta, \tag{8.4}$$

which describes exactly the combination of the initial field E_0 and the potential coming from the sphere's induced dipole moment:

$$p = 4\pi R^3 \varepsilon_0 \left(\frac{\varepsilon_1 - \varepsilon_2}{\varepsilon_1 + 2\varepsilon_2}\right) E_0. \tag{8.5}$$

Therefore, the polarizability, defined as the proportionality factor between the electric field and the dipole moment, induced by the same electric field, is:

$$\alpha = 4\pi R^3 \varepsilon_0 \left(\frac{\varepsilon_1 - \varepsilon_2}{\varepsilon_1 + 2\varepsilon_2}\right). \tag{8.6}$$

Appendix 8.C Quantum harmonic oscillator

Quantum harmonic oscillator (QHO) is the quantum analog of its classical counterpart. It is used as a model of a harmonic oscillator, which is the trapped particle in quantum regime. The Hamiltonian of QHO can be written as:

$$\hat{H}_{\mathrm{QHO}} = \frac{\hat{p}^2}{2m} + \frac{m\omega^2\hat{x}^2}{2}. \tag{8.7}$$

Position and momentum operators $\hat{x}$ and $\hat{p}$ can be represented through ladder operators, creation operator $\hat{a}^\dagger$ and annihilation operator $\hat{a}$:

$$\hat{x} = \frac{\hbar}{2m\omega}\left(\hat{a} + \hat{a}^\dagger\right) \tag{8.8a}$$

$$\hat{p} = i\frac{\hbar m\omega}{2}\left(\hat{a}^\dagger - \hat{a}\right), \tag{8.8b}$$

thus changing the Hamiltonian into:

$$\hat{H}_{\mathrm{QHO}} = \hbar\omega\left(\hat{a}^\dagger\hat{a} + \frac{1}{2}\right). \tag{8.9}$$

Appendix 8.D Position detection

We determine the particle's cavity position with three cameras, which image scattered light of the particle from the side of the cavity. The "main" camera is set to image the whole cavity, while the two other cameras image the space close to cavity mirrors. A clear view of this space is obstructed from the main camera by the mirror curvature and the construction of mirror holders. The fields of view between the side-cameras and the main camera are slightly overlapped. Figure 8.1 shows a trapped particle in two out of three pictures, which are taken simultaneously.

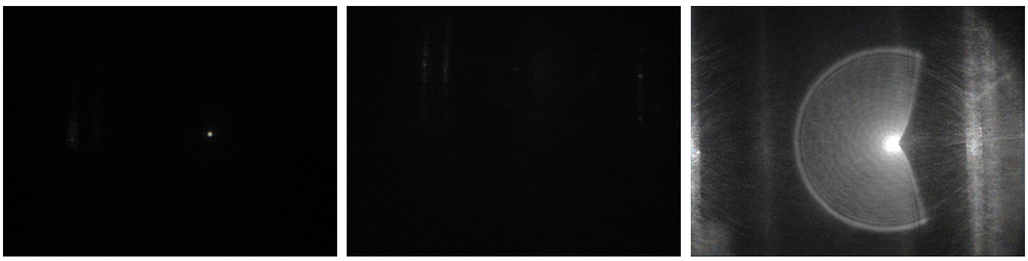

Figure 8.1: **Pictures from three cameras.** Pictures are taken simultaneously from three cameras with overlapping field of view. The first two pictures show the space close to cavity mirrors, which is not possible to observe on the third camera. The image of the particle in the third picture is clearly cut by the retaining ring holding the mirror. The same particle is also seen in the first picture.

The particle's position is extracted from the pictures by image processing in Mathematica. We first take pictures from all cameras without a trapped particle, which we subsequently subtract with `ImageSubtract` from the pictures with a particle, thus eliminating any scattered light which doesn't come from the particle. The result is then processed by a color filter `Binarize`, which creates a black and white picture. Stray white pixels left from other components can be filtered out by using the `DeleteSmallComponents` procedure. Using the `ComponentMeasurements` procedure, we extract the position of the particle. Figure 8.2 shows the procedure for the main camera, with the red circle showing the detected particle.

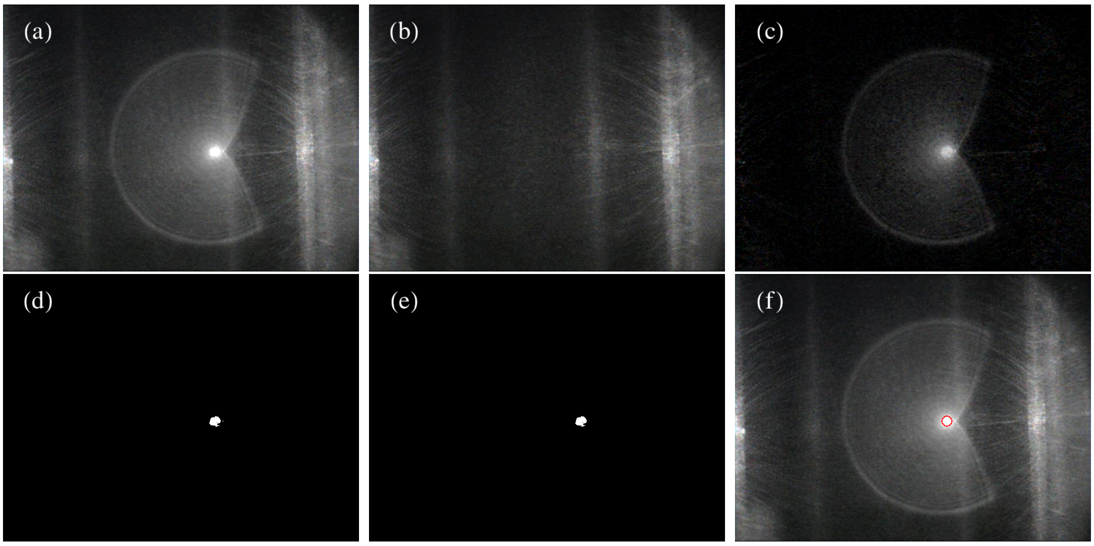

Figure 8.2: **Image processing from a single camera.** A picture of a cavity without a particle (b) is subtracted from a picture with a particle (a). The result (c) contains the scattered light mostly from the particle. The image is then turned from a grayscale image into a black and white image (d), with the parameter distinguishing the two set such that we remove the imaging rings from the particle. We use a procedure to filter out any stray pixels left (e). We then use a procedure that fits circles on an image, which outputs the center and the radius of the circle. We overlap the result (red circle) with a starting image (f) to see if the procedure gives good results.

The particle's position obtained by the image processing is given in pixels. In order to obtain the actual position, we fit a frequency dependence on the cavity position. We obtain the frequency from the NPS of the particle's motion, which we measure simultaneously to the taking of pictures. We move the particle along the cavity by heating it with the control beam for a short moment ($\sim 5s$).

The actual dependence we fit is given by the intensity profile (equation (2.23)), where the intensity is proportional to the square of the frequency (equation (3.24)):

$$\Omega_m(x) = \Omega_m^0 \sqrt{\frac{1}{1+\left(\frac{C_x(x_s - \text{off})}{x_R}\right)^2}}. \tag{8.10}$$

Ω_m^0 is the particle's frequency at the cavity center, off is the position of the cavity center in the picture (in pixels) and C_x is the pixels-to-meters conversion constant. For the fit, we take the positions taken from the main camera, as the particle can almost always be seen there. The fit and fit parameters can be seen in Figure 8.3. This fit can now be used to extract the actual position of the particle.

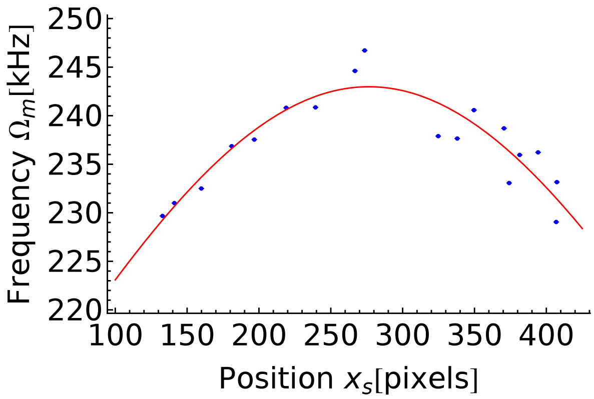

Fit parameter	Fit value
Ω_m^0[kHz]	243 ± 1
off[pix]	276 ± 4
$C_x \left[\frac{m}{\text{pix}}\right]$	$(12.2 \pm 0.8) \cdot 10^{-6}$

Figure 8.3: **Calibration of the position in the cavity.** We fit the experimental data (blue points) dependence of the frequency Ω_m on the particle's position in pixels (red line). The fit parameters, given in the table, give the calibration of the position in pixels to the actual position in meters.

Appendix 8.E Cavity cooling of an optically levitated nanoparticle

Cavity cooling of an optically levitated nanoparticle

Nikolai Kiesel,[1,*] Florian Blaser,[1,*] Uroš Delić,[1] David Grass,[1] Rainer Kaltenbaek,[1] and Markus Aspelmeyer[1]

[1] *Vienna Center for Quantum Science and Technology (VCQ), Faculty of Physics, University of Vienna, Boltzmanngasse 5, A-1090 Vienna, Austria*

The ability to trap and to manipulate individual atoms is at the heart of current implementations of quantum simulations [1, 2], quantum computing [3, 4], and long-distance quantum communication [5–8]. Controlling the motion of larger particles opens up yet new avenues for quantum science, both for the study of fundamental quantum phenomena in the context of matter wave interference [9, 10], and for new sensing and transduction applications in the context of quantum optomechanics [11, 12]. Specifically, it has been suggested that cavity cooling of a single nanoparticle in high vacuum allows for the generation of quantum states of motion in a room-temperature environment [13–15] as well as for unprecedented force sensitivity [16, 17]. Here, we take the first steps into this regime. We demonstrate cavity cooling of an optically levitated nanoparticle consisting of approximately 10^9 atoms. The particle is trapped at modest vacuum levels of a few millibar in the standing-wave field of an optical cavity and is cooled through coherent scattering into the modes of the same cavity [18, 19]. We estimate that our cooling rates are sufficient for ground-state cooling, provided that optical trapping at a vacuum level of 10^{-7} millibar can be realized in the future, e.g., by employing additional active-feedback schemes to stabilize the optical trap in three dimensions [20–23]. This paves the way for a new light-matter interface enabling room-temperature quantum experiments with mesoscopic mechanical systems.

Cooling and coherent control of single atoms inside an optical cavity are well-established techniques within atomic quantum optics [24–28]. The main idea of cavity cooling relies on the fact that the presence of an optical cavity can resonantly enhance scattering processes of laser light that deplete the kinetic energy of the atom, specifically those processes where a photon that is scattered from the atom is Doppler-shifted to a higher frequency. It was realized early on that such cavity-enhanced scattering processes can be used to achieve laser cooling even of objects without exploitable internal level structure such as molecules and nanoparticles [18, 19, 29, 30]. For nanoscale objects, cavity cooling has been demonstrated in a series of recent experiments with nanobeams [31–33] and membranes of nm-scale thickness (e.g. [34, 35]). To guarantee long interaction times with the cavity field these objects were mechanically clamped, which however introduces additional dissipation and heating through the mechanical support structure. As one consequence, quantum signatures have thus far only been observed in a cryogenic environment [36, 37]. Freely suspended particles can circumvent this limitation and allow for far better decoupling of the mesoscopic object from the environment. This has been successfully implemented for atoms driven at optical frequencies far detuned from the atomic resonances, both for the case of optically trapped single atoms [26, 27] and for clouds of up to 10^5 ultracold atoms [38–40]. In contrast to such clouds, massive solid objects provide access to a new parameter regime: on the one hand, the rigidity of the object allows to manipulate the center-of-mass motion of the whole system, thus enabling macroscopically distinct superposition states [14, 15, 41]; on the other hand the large mass density of solids concentrates many atoms in a small volume of space, which provides new perspectives for force sensing [16, 17]. In our work, we have now extended the scheme to dielectric nanoparticles comprising up to 10^9 atoms. By using a high-finesse optical cavity for both optical trapping and manipulation we demonstrate, for the first time, cavity-optomechanical control, including cooling, of the center-of-mass (CM) motion of a levitated solid object without internal level structure.

To understand the principle of our approach, consider a dielectric spherical particle of radius r smaller than the optical wavelength λ. Its finite polarizability $\xi = 4\pi\epsilon_0 r^3 Re\left\{\frac{\epsilon-1}{\epsilon+2}\right\}$($\epsilon$: dielectric constant; ϵ_0: vacuum permitivity) results in an optical gradient force that allows to trap particles in the intensity maximum of an optical field [42]. The spatial modes of an optical cavity provide a standing-wave intensity distribution along the cavity axis x. A nanoparticle that enters the cavity will be pulled towards one of the intensity maxima, located a distance x_0 from the cavity center. For the case of a Gaussian (TEM00) cavity mode, the spatial profile will result in radial trapping around the cavity axis, hence providing a full 3D particle confinement. In addition, Rayleigh scattering off the particle into the cavity mode induces a dispersive change in optical path length and shifts the cavity resonance frequency by $U_0(x_0) = \frac{\omega_{cav}\xi}{2\epsilon_0 V_{cav}}\left(1 + \frac{x_0^2}{x_R^2}\right)$ [43](ω_{cav}: cavity frequency; V_{cav}: cavity mode volume; x_R: cavity-mode Rayleigh length). This provides the underlying optomechanical coupling mechanism between the CM motion of a particle moving along the cavity axis and the photons of a Gaussian cavity mode. The result-

*These authors contributed equally to this work.

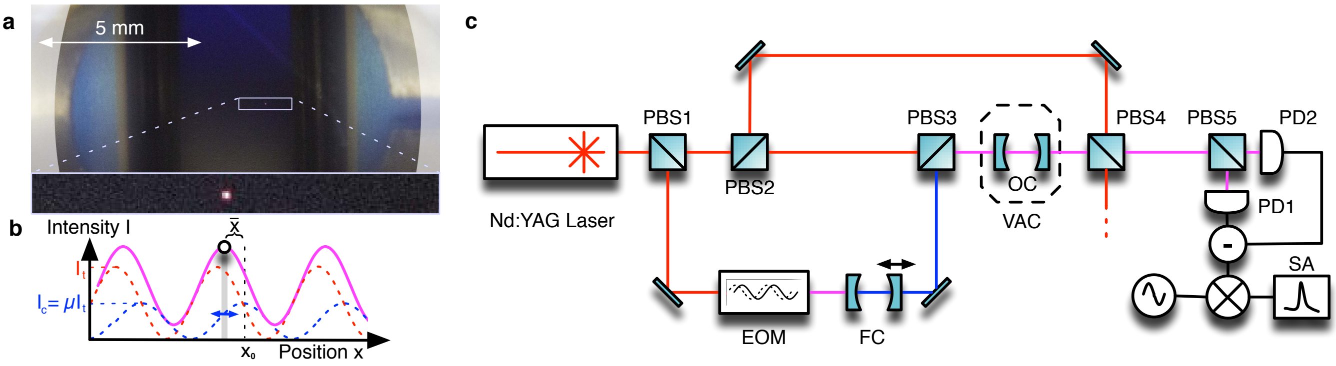

FIG. 1: **Optical trapping and readout of a nanoparticle in a Fabry-Perot cavity. (a) Nanoparticle in a cavity.** A photo of our near-confocal Fabry-Perot optical cavity (OC) (F=76000; $L = \frac{c}{2\mathrm{FSR}}$ =10.97 mm, determined via the free spectral range FSR). The white-shaded areas indicate the curvature of the cavity mirrors. The optical field between the mirrors traps a nanoparticle. The enlarged inset shows light scattered by the nanoparticle. **(b) Schematics of two-mode optical trap and dispersive coupling.** Two optical fields form standing-wave intensity distributions along the optical cavity axis (dashed lines; blue: control beam; red: trapping beam). Because of their different frequencies, the intensity maxima of the two fields are displaced with respect to each other. A nanoparticle is trapped at the maximum of the total intensity distribution (purple solid line). Since the trapping beam is more intense than the control beam, the nanoparticle is trapped at a distance $\overline{x} \neq 0$ away from the control-beam intensity maximum x_0. As a consequence, the nanoparticle oscillates within a region where the control-beam intensity varies with the particle position (blue arrow), resulting in linear dispersive coupling (see main text and appendix). The displacement $\overline{x}$ depends on the ratio between the intensity maxima of the two fields **(c) Experimental setup.** A Nd:YAG laser ($\lambda = 1064$ nm) is split into three beams at the polarizing beam splitters PBS1 and PBS2 (for simplicity waveplates not shown in the figure). The transmitted beam is used to lock the laser to the TEM00 mode of the OC and provides the trapping field for the nanoparticle. The beam reflected at PBS1 is used to prepare the control beam, which is frequency-shifted by $\delta\omega$ close to the adjacent cavity resonance of the TEM00 mode, i.e., $\delta\omega$=FSR + Δ (Δ: detuning from cavity resonance). The single-frequency sideband at $\delta\omega$ is created using an electro-optical modulator (EOM) followed by optical amplification in fiber (not shown) and transmission through a filtering cavity (FC) with an FWHM linewidth of $2\pi\times500$ MHz. The control and trapping beams are overlapped at PBS3 and transmitted through the OC with orthogonal polarizations. The OC is mounted inside a vacuum chamber (VAC). When a nanoparticle is trapped in the optical field in the cavity, its center-of-mass (CM) motion introduces a phase modulation on the control beam. To detect this signal, we perform interferometric phase readout of the control beam: At PBS4 the trapping beam is separated from the control beam and overlapped with the local oscillator (LO). After rotating the polarization, the control beam and the LO are mixed at PBS 5. High-frequency InGaAs photo detectors PD1 and PD2 detect the light in both output ports of PBS5. We mix the difference signal of the two detectors with an electronic local oscillator of frequency FSR + Δ and record the noise power spectrum of resulting signal at a spectrum analyzer (SA) (see Methods).

ing interaction Hamiltonian is

$$H_{int} = -\hbar U_0(x_0)\hat{n}\sin^2(kx_0 + k\overline{x} + k\hat{x}),$$

where we have allowed for a mean displacement $\overline{x}$ of the nanoparticle with respect to the intensity maximum x_0 ($\hat{x}$: CM position operator of the trapped nanoparticle; $k=\frac{2\pi}{\lambda}$: wavenumber of the cavity light field; $\hat{n}$: cavity photon number operator). For the case of a single optical cavity mode, the particle is trapped at an intensity maximum ($\overline{x} = 0$) and, for small displacements, only coupling terms that are quadratic in $\hat{x}$ are relevant [34]. Linear coupling provides intrinsically larger coupling rates and can be exploited for various quantum control protocols [44]. However, it requires to position the particle outside the intensity maximum of the field. This can be achieved for example by an optical tweezer external to the cavity [14], by harnessing gravity in a vertically mounted cavity [45] or by using a second cavity mode with longitudinally shifted intensity maxima [13, 14].

We follow the latter approach and operate the optical cavity with two longitudinal Gaussian modes of different frequency, namely, a strong "trapping field" to realize a well-localized optical trap at one of its intensity maxima, and a weaker "control field" that couples to the particle at a shifted position $\overline{x} \neq 0$. For localization in the Lamb-Dicke regime ($k^2\langle\hat{x}^2\rangle \ll 1$) this yields [12, 46] linear optomechanical coupling between the trapped particle and the control field at a rate $g_0 = U_0(x_0)\sin(2k\overline{x})k\sqrt{\frac{\hbar}{m\Omega_0}}$ per photon (m: nanoparticle mass; Ω_0: frequency of CM motion). Detuning of the control field from the cavity resonance by a frequency $\Delta = \omega_{cav} - \omega_c (\omega_c$: control field frequency) results in the well-known dynamics of cavity optomechanics [12]. Specifically, the position dependence of the gradient force will change the stiffness of the optical trap, shifting Ω_0 to an effective frequency Ω_{eff} (optical spring), and the cavity-induced retardation of the force will introduce additional optomechanical (positive or negative) damping on the particle motion. From a quantum-optics viewpoint, the oscillating nanoparti-

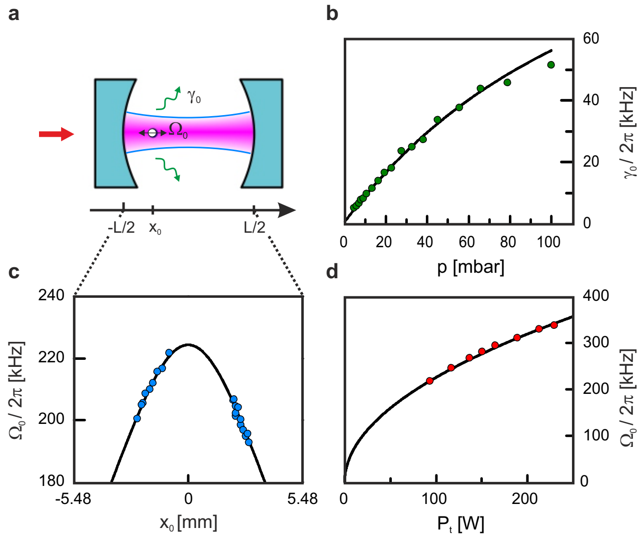

FIG. 2: **Experimental characterization of the nanoparticle cavity trap . (a) Schematic of the trap configuration.** An optical cavity of length $L = 10.97$ mm is driven on resonance of a Gaussian TEM00 cavity mode by a laser with a wavelength of $\lambda = 1064$ nm. The nanoparticle is optically trapped at position x_0. Its center-of-mass motion in the axial direction of the cavity is described by a harmonic oscillator with a frequency Ω_0 and an amplitude of approximately 10 nm . In addition, the nanoparticle experiences collisions with the surrounding gas resulting in a damping rate γ_0. **(b) Mechanical damping γ_0 as a function of pressure**. The solid line is a fit of kinetic gas theory to the data (see appendix D). **(c) Position-dependent trapping frequency.** The waist of the optical mode expands from approximately $41\mu m$ at the cavity center to $61\mu m$ at the cavity mirrors, resulting in a position-dependent trapping potential. Here, we show the corrsponding change of the trapping frequency Ω_0 with the position of the nanoparticle. **(d) Power-dependent trapping frequency.** We experimentally show the dependence of the trapping frequency on the intracavity power P_{t}. The solid lines in Fig. **c, d** are based on the theoretical model as described in the main text, with a scaling factor as the only free fit parameter.

cle scatters photons into optical sidebands of frequencies $\omega_{\mathrm{c}} \pm \Omega_0$ at rates $A_{\pm} = \frac{1}{4}\frac{g_0^2\langle\hat{n}\rangle\kappa}{(\kappa/2)^2+(\Delta\pm\Omega_0)^2}$, known as Stokes and anti-Stokes scattering, respectively (κ: FWHM cavity linewidth). For $\Delta > 0$ (red detuning) anti-Stokes scattering becomes resonantly enhanced by the cavity, effectively depleting the kinetic energy of the nanoparticle motion via a net laser-cooling rate of $\Gamma = A_- - A_+$. In the following, we demonstrate all these effects experimentally with an optically trapped silica nanoparticle.

As is shown in Figure 1, our setup comprises a high-finesse Fabry-Perot cavity (Finesse $F = 76000$; $\kappa = 2\pi \times 180$ kHz) that is mounted inside a vacuum chamber kept at a pressure between 1 and 5 mbar. Airborne silica nanoparticles (specified with radius $r = 127 \pm 13$ nm) are emitted from an isopropanol solution via an ultrasonic nebulizer and are trapped inside the cavity in the standing wave of the trapping field (see Methods Section). To achieve the desired displacement between the intensity maxima of trapping field and control field ($\overline{x} \neq 0$), we use the adjacent longitudinal cavity mode for the control beam, i.e. the cavity mode shifted by approximately one free spectral range FSR $= \frac{c}{2L} \approx 13.67$ GHz in frequency from the trapping beam (c: vacuum speed of light; L: cavity length). Depending on the distance from the cavity center x_0, the two standing-wave intensity distributions are then shifted with respect to each other by $\frac{\lambda}{2L}(x_0 + L/2)$ (Figure 1c). For example, to achieve maximal coupling g_0 for weak control beam powers, i.e. for $\mu = \frac{P_c}{P_t} \ll 1$ ($P_{\mathrm{c(t)}}$: Power of control (trapping) beam in the cavity), the nanoparticle needs to be positioned at $x_0 = L/4$, where the antinodes of the two beams are separated by $\lambda/8$ [13, 14]. Note that when the control beam is strong enough to significantly contribute to the optical trap ($\mu \gtrapprox 0.1$), the displacement $\bar{x}$ and both Ω_0 and g_0 are modified when μ is changed [39] . The exact dependence of these optomechanical parameters on μ depends on x_0 (see appendix A and [47, 48]).

The optomechanical coupling between the control field and the particle can be used to both manipulate and detect the particle motion. Specifically, the axial motion of the nanoparticle generates a phase modulation of the control field, which we detect by heterodyne detection (see methods section). We reconstruct the noise power spectrum (NPS) of the mechanical motion by taking into account the significant filtering effects exhibited by the cavity (arising from the fact that $\kappa \approx \Omega_0$) on the transmitted control beam ([49] and appendix A). The inferred position sensitvity of our readout scheme for a nanoparticle of approx. 170 nm radius is 4 pm/$\sqrt{\mathrm{Hz}}$, which is likely limited by classical laser noise (see below).

The properties of our optical trap are summarized in Figure 2. The influence of the control beam on the trapping potential is purposely kept small by choosing $\mu \approx 0.1$ and $\Delta \approx 0$. We expect that the axial mechanical frequency Ω_0 depends both on the power of the trapping beam P_{t} and on x_0 through the cavity beam waist $W(x_0)$ via $\Omega_0 = \sqrt{\frac{12k^2}{c\pi}Re(\frac{1}{\rho}\frac{\epsilon-1}{\epsilon+2})} \cdot \sqrt{\frac{P_{\mathrm{t}}}{\pi W(x_0)}}$ [13, 14], in agreement with our data. The damping γ_0 of the mechanical resonator is dominated by the ambient pressure of the background gas down to a few millibar (Fig. 1c). Below these pressures the nanoparticle is not stably trapped anymore, while trapping times up to several hours can be achieved at a pressure of a few millibar. This is a known, yet unexplained phenomenon [21, 22, 47]. Reproducible optical trapping at lower pressure values has thus far only been reported using feedback cooling in three dimensions for the case of nanoparticles [21, 22] or, without feedback cooling, with particles of at least 20 μm radius [50].

We finally demonstrate cavity-optomechanical control of our levitated nanoparticle. All measurements have been performed with the same particle for an intra-cavity trapping beam power P_t of approx. 55 W and at a pres-

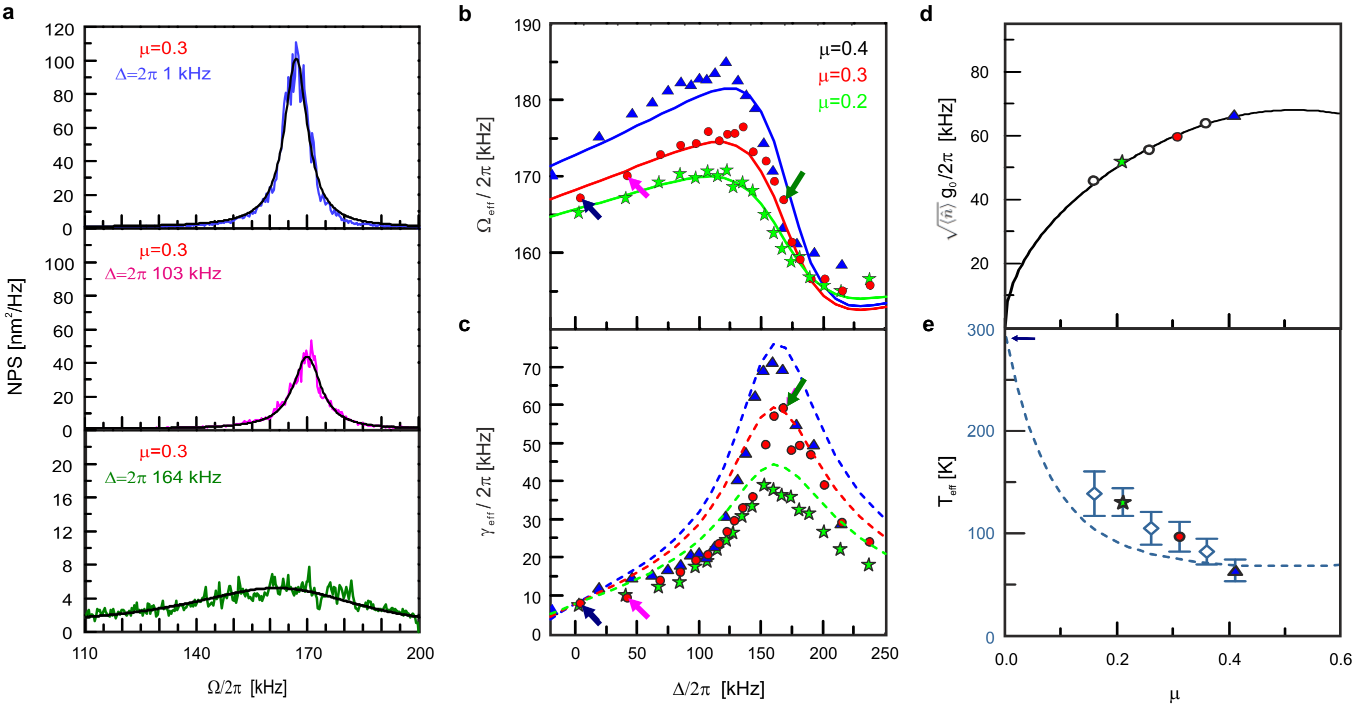

FIG. 3: **Cavity-optomechanical control and cooling of a nanoparticle.** We obtain noise power spectra (NPS, see panel (a)) of the nanoparticle's center-of-mass motion for different settings of the control-beam power P_c and detuning Δ. During each measurement, $\mu = \frac{P_c}{P_t}$ was kept constant (P_t: trapping beam power). Based on these NPS, we determine the effective mechanical frequency Ω_{eff} and linewidth γ_{eff} of the optomechanical system, and its effective temperature T_{eff}. We study the modification of these spectra caused by optomechanical interaction in panels (b), (c) and (e). Based on the data in panel (b) we infer the power-dependent strength of optomechanical coupling in panel (d). **(a) Mechanical noise power spectra.** Shown are examples of the mechanical NPS measured for constant control-beam power ($\mu = 0.3$) at three different detunings Δ with respect to the cavity resonance frequency. The detuning results in a significant modification of the NPS due to optomechanical effects. Note that scale is changed by a factor of 5 in the bottom plot in panel (a). In order to determine the effective mechanical frequency Ω_{eff} and linewidth γ_{eff} of the optomechanical system, we fit the NPS of an harmonic oscillator (black solid lines) to this data. We infer the value of the effective temperature T_{eff} from the equipartition theorem via direct integration of the NPS (see appendix C). **(b) Optical spring.** When the control beam is red-detuned from the cavity resonance ($\Delta > 0$), we observe a characteristic modification of the mechanical frequency Ω_{eff}. The solid lines in (b) correspond to a theoretical model that is fitted to the data for each value of μ. The optomechanical coupling $g_0\sqrt{\langle \hat{n} \rangle}$ is one of the fit parameters (see appendix C). Based on these results for the optical spring, we calculate the theoretical expectations for γ_{eff} and T_{eff}, which are shown as dashed lines in panels (c) and (e). **(c) Optomechanical damping**. Linewidth broadening of the mechanical resonance as a function of the detuning Δ. **(d) Optomechanical coupling.** We infer the optomechanical coupling rate $g_0\sqrt{\langle \hat{n} \rangle}$ from the strength of the optical spring (panel (b)) and show its dependence on the power ratio μ. This relation depends on the position x_0 of the nanoparticle in the cavity. For the data presented here, we determine $x_0 = 1.56 \pm 0.14$ mm (see appendix E). We find very good agreement between the data and the theoretical model, where only the nanoparticle polarizability serves as a fit parameter (solid line; also see appendix C). **(e) Cavity cooling.** The decrease in effective temperature T_{eff} is shown for increasing control-beam power. To obtain a good estimate of the measurement error, we average over measurements taken for detunings between $\Delta = 100 - 150$ kHz (see appendix C). The dashed line is a theoretical prediction based on the parameters obtained from the fit to the optical spring data (panel (b)).

sure of $p \approx 4$ mbar. This corresponds to a bare mechanical frequency $\Omega_0/2\pi = 165 \pm 3$ kHz and an intrinsic mechanical damping rate $\gamma_0/2\pi = 7.2 \pm 0.8$ kHz, respectively. Figure 3a shows the dependence of a typical noise power spectrum (NPS) of the particle's motion upon detuning of the control field. Note that the power ratio μ between trapping beam and control beam is kept constant, which is achieved by adjusting the control-beam power for different detunings. The amplitude scale, as well as the temperature scale in Figure 3e, is calibrated through the NPS measurement performed close to zero detuning ($\Delta = 1$ kHz; blue NPS in Fig. 3a by using the equipartition theorem for $T = 293K$. This is justified by an independent measurement that verifies thermalization of the center of mass (CM) mode at zero detuning for our parameter regime (see appendix D). Both the inferred effective mechanical frequency Ω_{eff} (Figure 3b and the effective mechanical damping γ_{eff} (Figure 3c show a systematic dependence on the detuning Δ of the control beam, in good agreement with the expected dynamical backaction effects for linear optomechanical coupling (see appendix A). A fit of the expected theory curve to the optical spring data allows estimating the strength of the optomechanical coupling for different values of μ (Figure 3d). If the position x_0 of the nanoparticle in the cavity is known, then this behaviour is uniquely determined by $U_0(x_0)$. For a particle position $x_0 = 1.56 \pm 0.14$ mm, which was determined independently with a CCD camera, we find $U_0(x_0) = 2\pi \times (145 \pm 2)$ kHz. These values allow to infer a nanoparticle displacement $\overline{x} \approx 0.15 \times (\lambda/2) = 77$ nm, yielding a fundamental single-photon coupling rate $g_0 \approx 2\pi \times 1.2$ Hz (for $\mu \to 0$). Assuming a (supplier specified) material density of $\rho = 1950$ g/cm^{3}and a dielectric constant $\epsilon_{\mathrm{SiO_2}} = 2.1$, our results indicate a single trapped nanoparticle of radius $r \approx 169$ nm.

The red-detuned driving of the cavity by the control laser also cools the CM motion of the levitated nanoparticle through coherent scattering into the cavity modes. Figure 3e shows the resulting effective temperature as deduced from the area of the NPS of the mechanical motion by applying the equipartition theorem. The experimental data is well in agreement with the expected theory for cavity cooling (see appendix A). We achieve cooling rates of up to $\Gamma = 2\pi \times 49$ kHz and effective optomechanical coupling rates of up to $g_0\sqrt{\langle \hat{n}_c \rangle} = 2\pi \times 66$ kHz ($\langle \hat{n}_c \rangle$: mean photon number in control field), comparable to state-of-the-art clamped mechanical systems in that frequency range [12]. The demonstrated cooling performance, with a minimal CM-mode temperature of 64 ± 5 K, is only limited by damping through residual gas pressure that results in a mechanical quality of $Q = \frac{\Omega_0}{\gamma_0} \approx 25$. Recent experiments [21, 22] impressively demonstrate, that lower pressures can be achieved when cooling is applied in all three spatial dimensions. Given the fact that our cavity-induced longitudinal cooling rate is comparable to the feedback cooling rates achieved in those experiments, a combined scheme should eventually be capable of performing quantum experiments at moderately high vacuum levels. For example, our cooling rate is in principle sufficient to obtain cooling to the quantum ground state of the CM-motion starting from room temperature with a longitudinal mechanical quality factor of $Q \approx 10^9$, i.e., a vacuum level of 10^{-7} mbar. Such a performance is currently out of reach for other existing cavity optomechanical systems with comparable frequencies. In addition, even larger cooling rates are expected when both beams are red-detuned to cooperatively cool the nanoparticle motion [47].

Our experiment constitutes a first proof of concept demonstration in that direction. We envision that once this level of performance is achieved levitated nanoparticles in optical cavities will provide a room-temperature quantum interface between light and matter, along the lines proposed in [13, 14, 44, 51], with new opportunities for macroscopic quantum experiments in a regime of large mass [15, 41, 52]. The large degree of optomechanical control over levitated objects may also enable applications in other areas of physics such as for precision force sensing [16, 17] or for studying non-equilibrium dynamics in classical and quantum many-body systems [53].

Acknowledgements

We would like to thank O. Romero-Isart, A. C. Pflanzer, J. I. Cirac, P. Zoller, H. Ritsch, C. Genes, S. Hofer, G. D. Cole, W. Wieczorek, M. Arndt, T. Wilk for stimulating discussions and support and J. Schmöle for his graphical contributions. We acknowledge funding from the Austrian Science Fund FWF (START, SFB FOQUS), the European Commission (IP Q-ESSENCE, ITN cQOM), the European Research Council (ERC StG QOM), the John Templeton Foundation (RQ-8251) and the European Space Agency (AO/1-6889/11/NL/CBi). N. K. acknowledges support by the Alexander von Humboldt Stiftung. U. D., D. G. acknowledge support by the FWF through the Doctoral Programme CoQuS. R. K. acknowledges support from the Austrian Academy of Sciences (APART) and the European Commission (Marie Curie). M. A. and R. K. acknowledge support through the Keck Institute for Space Studies.

Author Information

Correspondence and requests for materials should be addressed to N. K. (e-mail: nikolai.kiesel@univie.ac.at) or M. A. (e-mail: markus.aspelmeyer@univie.ac.at).

Methods

Loading of nanoparticles into the optical cavity trap

For our experiment we use silica nanospheres (Corpuscular Inc.) with a radius of $r = 127 \pm 13$ nm , which are provided in an aqueous solution with a mass concentration of 10%. We dilute the solution with isopropanol to a mass concentration of 10^{-7} and keep it for approximately 30 min in an ultrasonic bath before usage. To obtain airborne nanoparticles, an ultrasonic medical nebulizer (Omron Micro Air) emits droplets from the solution with approximately 3μm size [48, 54]. On average, the number of nanospheres per droplet is then approximately $5 \cdot 10^{-4}$.

The nanospheres are loaded into the vacuum chamber by spraying the droplets through an inlet valve at the end of a 6mm thick, 90cm long steel tube. We keep the pressure inside the vacuum chamber between 1 and 5 mBar via manual control of both the inlet valve connected to the nebulizer and the outlet valve connected to the vacuum pumps. During the loading process, the trapping laser is kept resonant with the cavity at the desired intracavity power for optical trapping. The low pressure minimizes pressure-induced fluctuations of the optical path length, which significantly simplifies locking the laser to the cavity.

Trapping in the conservative potential of the standing-wave trap is only possible with an additional dissipative process, which is provided fully by damping due to the remaining background gas. Within a few seconds after opening the valve, nanospheres get optically trapped. The standing-wave configuration provides multiple trapping positions. Trapped nanoparticles are detected by a CCD-camera, which is also used to determine their position x_0 (see appendix E). If initially more than one position in the cavity is occupied, blocking the trapping beam for short intervals allows loosing surplus particles for our measurements. To move the trapped particle to different positions along the cavity, we blue-detune the control laser to heat the CM degree of freedom of the particle. The "hot" particle moves across the standing wave until the control beam is switched off and the particle stays trapped at its new position (see Figure 2b).

Readout of control beam

For the position readout of the nanoparticle motion, we rely on the dispersive interaction with the control-field cavity mode. The control laser beam is initially prepared with a frequency difference of $\delta\omega \approx 2\pi \times 13.67$ GHz with respect to the original laser frequency ω_0. When the control beam is transmitted through the cavity, it experiences a phase shift according to its detuning from the resonance ω_{cav}. Because the particle position in the cavity modifies the cavity resonance frequency ω_{cav}, a phase readout of the transmitted control beam allows reconstructing the nanoparticle's motion. To detect the phase modulation introduced by the particle motion along the cavity, we first mix the control beam with a local oscillator (LO, 3.15 mW; control beam power $<$ 0.1mW) at frequency ω_0 at PBS5 (Fig. 1). In the output ports of PBS5, we then detect the optical signal at photodetectors PD1 and PD2 (Discovery Semiconductor Inc. DSC-R410), which are fast enough to process the beat signal at frequency $\delta\omega$. Their difference signal $l(t)$, i.e., the heterodyne measurement outcome, contains the beat signal, whose phase ϕ_{opt} is determined by the unknown path difference between the LO and the control beam. The beat signal carries sidebands representing the amplitude and phase modulation imprinted on the control beam by the optomechanical system. We demodulate $l(t)$ with an electronic local oscillator (ELO) with frequency $\delta\omega$ and phase ϕ_{ELO} (relative to the beat signal). From the resulting signal $s_{\mathrm{opt}}(t)$, we extract the phase modulation of $l(t)$ by adjusting ϕ_{ELO} such that the total phase $\phi_{\mathrm{ELO}} + \phi_{\mathrm{opt}} = \pi/2$. This is achieved by locking the DC part of $\langle s_{\mathrm{opt}}(t)\rangle$ to zero. We record the NPS of $s_{\mathrm{opt}}(t)$ with a spectrum analyzer, which allows reconstructing the NPS of the nanoparticle's motion in post processing.

Appendix A: Description of the Optomechanical System

Optomechanical Hamiltonian

To describe our experiment theoretically, we consider a nanoparticle that is optically trapped within a Fabry-Perot cavity. Two laser beams drive adjacent TEM_{00} cavity modes. One beam is used for optical trapping (trapping beam), the other for optomechanical control and readout of the nanoparticle center-of-mass motion (control beam). The two mode's resonance frequencies differ by one $\mathrm{FSR} = \frac{c}{2L}$ (L: cavity length). In the most general case, the two lasers can be detuned from the respective cavity resonance frequency by Δ_t and Δ_c ($\Delta_{c(t)}$: detuning of the control (trapping) beam). The system is described using the following Hamiltonian [48]:

$$\begin{aligned}\hat{H}/\hbar \;&=\; \Delta_t \hat{a}_t^\dagger \hat{a}_t + \Delta_c \hat{a}_c^\dagger \hat{a}_c + \frac{\hat{p}_m^2}{2m\hbar} - U_0 \hat{a}_t^\dagger \hat{a}_t \sin^2(k_t \hat{x}) \\ &\quad - U_0 \hat{a}_c^\dagger \hat{a}_c \sin^2(k_c \hat{x}) + iE_t(\hat{a}_t^\dagger - \hat{a}_t) + iE_c(\hat{a}_c^\dagger - \hat{a}_c),\end{aligned} \tag{A1}$$

where U_0 can be understood as the cavity resonance frequency shift introduced by a nanoparticle that is located at the intensity maximum at the center of the optical cavity. At the same time, $\hbar U_0$ is also the trap depth created by a single intracavity photon ($\hat{a}_{c(t)}^\dagger$ / $\hat{a}_{c(t)}$: creation/annihilation operator of the control (trapping) field in the cavity; m: mass of the nanoparticle; $\hat{x}$ ($\hat{p}_m$): position (momentum) operatior of the nanoparticle's CM; $k_{c(t)}/E_{c(t)}$: wavenumber/driving field of the control (trapping) beam).

Given $|k_t - k_c| \ll k_c$, one can regard $(k_t - k_c)\hat{x}$ as a position-dependent phase shift between the standing waves of the two intracavity fields via $\sin^2(k_t\hat{x}) = \sin^2\left(k_c\hat{x} + (k_t - k_c)\hat{x}\right) = \sin^2\left(k_c\hat{x} + \varphi\right)$, where

$$\varphi = (k_t - k_c)x_0' = \frac{2\pi\mathrm{FSR}}{c}x_0' = \frac{\pi}{L}x_0'$$

We include the dependence on k_t in φ and use k instead of k_c from this point on. Further, we rewrite the position operator $\hat{x}$ as the sum of three terms: $\hat{x} = x_0' + \bar{x} + \hat{x}_m$, where x_0' is the position of the intensity maximum of the control field with respect to the cavity mirror ($\bar{x}$: the nanoparticle's mean displacement from x_0', $\hat{x}_m$: the nanoparticle's displaced position operator with $\langle \hat{x}_m \rangle = 0$). Note that in the main text we always use the distance from the cavity center x_0, where $x_0' = x_0 + L/2$. We also introduce the dimensionless position operator $\delta\hat{x}$ with $\hat{x}_m = X_{\mathrm{gs}} \cdot \delta\hat{x}$, where $\delta\hat{x} = \frac{1}{\sqrt{2}}(\hat{b} + \hat{b}^\dagger)$ (X_{gs}: Ground state extension of the mechanical oscillator, $b^{(\dagger)}$: CM-motion annihilation (creation) operator).

We approximate the trigonometric functions in equation A1 to a second-order in $\hat{x}_m$ and perform a displacement operation of the light operators: $\hat{a}_j \to \alpha_j + \hat{a}_j$ about their steady-state mean values α_t and α_c. The Hamiltonian after these modifications is:

$$\begin{aligned}
\frac{H}{\hbar} &= \Delta_t|\alpha_t|^2 + \Delta_c|\alpha_c|^2 + \Delta_t\alpha_t(\hat{a}_t + \hat{a}_t^\dagger) + \Delta_c\alpha_c(\hat{a}_c + \hat{a}_c^\dagger) + \Delta_t\hat{a}_t^\dagger\hat{a}_t + \Delta_c\hat{a}_c^\dagger\hat{a}_c \\
&+ \frac{\hat{p}_m^2}{2m\hbar} - U_0|\alpha_t|^2\sin^2(k(x_0'+\bar{x})+\varphi) - U_0|\alpha_c|^2\sin^2(k(x_0'+\bar{x})) \\
&- 2U_0k^2|\alpha_t|^2\cos(2k(x_0'+\bar{x})+2\varphi)\frac{\hat{x}_m^2}{2} - 2U_0k^2|\alpha_c|^2\cos(2k(x_0'+\bar{x}))\frac{\hat{x}_m^2}{2} \\
&- U_0k\alpha_t\sin(2k(x_0'+\bar{x})+2\varphi)(\hat{a}_t+\hat{a}_t^\dagger)\hat{x}_m - U_0k\alpha_c\sin(2k(x_0'+\bar{x}))(\hat{a}_c+\hat{a}_c^\dagger)\hat{x}_m \\
&- U_0|\alpha_t|^2k\sin(2k(x_0'+\bar{x})+2\varphi)\hat{x}_m - U_0|\alpha_c|^2k\sin(2k(x_0'+\bar{x}))\hat{x}_m \\
&- U_0\alpha_t\sin^2(k(x_0'+\bar{x})+\varphi)(\hat{a}_t+\hat{a}_t^\dagger) - U_0\alpha_c\sin^2(k(x_0'+\bar{x}))(\hat{a}_c+\hat{a}_c^\dagger) \\
&+ iE_t(\hat{a}_t^\dagger - \hat{a}_t) + iE_c(\hat{a}_c^\dagger - \hat{a}_c).
\end{aligned} \tag{A2}$$

Line A2 takes the form of a harmonic potential $\frac{m\Omega_0^2\hat{x}_m^2}{2\hbar}$ with mechanical frequency Ω_0:

$$\Omega_0^2 = -\frac{2\hbar U_0 k^2}{m}\left(|\alpha_t|^2\cos(2k(x_0'+\bar{x})+2\varphi) + |\alpha_c|^2\cos(2k(x_0'+\bar{x}))\right). \tag{A3}$$

Line A2 determines the linear dispersive coupling of the nanosphere CM motion to the trapping and cooling beam. Note that the trapping beam also shows linear coupling when the cooling beam is strong enough to significantly contribute to the optical trap:

$$\begin{aligned}
g_{0,t} &= \zeta_t \cdot X_{\mathrm{gs}} = U_0kX_{\mathrm{gs}}\sin 2(k(x_0'+\bar{x})+\varphi) \\
g_{0,c} &= \zeta_c \cdot X_{\mathrm{gs}} = U_0kX_{\mathrm{gs}}\sin 2k(x_0'+\bar{x}).
\end{aligned} \tag{A4}$$

Note that we use $g_0 = g_{0,c}$ in the main text. To study the dynamics of the system, we solve the Langevin equations for both light fields:

$$\begin{aligned}
\dot{\hat{a}}_t &= -(\frac{\kappa}{2} + i(\Delta_t - U_0\sin^2(k(x_0'+\bar{x})+\varphi))(\hat{a}_t+\alpha_t) + E_t - \zeta_t\alpha_t\hat{x}_m \\
\dot{\hat{a}}_c &= -(\frac{\kappa}{2} + i(\Delta_c - U_0\sin^2 k(x_0'+\bar{x}))(\hat{a}_c+\alpha_c) + E_c - \zeta_c\alpha_c\hat{x}_m
\end{aligned} \tag{A5}$$

The additional loss terms account for the cavity amplitude decay rate κ. The value of κ is assumed to be equal for both light fields due to the small difference in their wavelengths. For the steady-state solutions of $\hat{a}_t$ and $\hat{a}_c$ we find:

$$\begin{aligned}
\alpha_t &= \frac{E_t}{\frac{\kappa}{2} + i(\Delta_t - U_0\sin^2 k(x_0'+\bar{x})+\varphi)} \\
\alpha_c &= \frac{E_c}{\frac{\kappa}{2} + i\left(\Delta_c - U_0\sin^2(k(x_0'+\bar{x}))\right)}.
\end{aligned} \tag{A6}$$

In our experiment, the Pound-Drever-Hall feedback loop keeps the trapping-laser frequency resonant to the corresponding cavity resonance frequency when the particle is in its steady state position. In other words, the detuning Δ_t compensates the frequency shift caused by the particle such that $\Delta_t - U_0\sin^2(k(x_0'+\bar{x})+\varphi) = 0$.

On the other hand, the frequency of the control beam is varied throughout the experiment. We are interested in the detuning Δ of the control beam with respect to the cavity resonance when the nanoparticle is located at its steady state position: $\Delta = \Delta_c - U_0\sin^2 k(x_0'+\bar{x})$.

The trapping beam power is not changed throughout the experiment. In contrast, the control beam power is always set to achieve the desired ratio between the power of the two intracavity fields μ:

$$\mu = \frac{|\alpha_c|^2}{|\alpha_t|^2} = \frac{|E_c|^2}{|E_t|^2}\frac{\left(\frac{\kappa}{2}\right)^2}{\left(\frac{\kappa}{2}\right)^2 + \Delta^2}. \tag{A7}$$

Heisenberg's equation of motion for the particle becomes:

$$\ddot{\hat{x}}_m + \Omega_0^2(\mu)\hat{x}_m = \frac{\hbar k U_0}{m}\left[|\alpha_t|^2 \sin 2(k(x_0' + \bar{x}) + \varphi) + |\alpha_c|^2 \sin 2k(x_0' + \bar{x})\right] - \gamma_m \dot{\hat{x}}_m \tag{A8}$$

where we included an additional damping term $\gamma_m \dot{\hat{x}}_m$, which is due to the collisions of the nanoparticle with the surrounding gas.

From Equation A8 we find a steady state condition on $x_0' + \bar{x}$, that enables us to determine the mechanical frequency Ω_0 and the displacement $\bar{x}$ as a function of μ:

$$\begin{aligned} \Omega_0^2(\mu) &= \Omega_0^2(0)\sqrt{1 + \mu^2 + 2\mu\cos 2\varphi} \\ \tan 2k\bar{x} &= -\frac{\sin 2\varphi}{\mu + \cos 2\varphi}. \end{aligned} \tag{A9}$$

Thereby, the mechanical frequency in absence of the cooling beam is (equation A3):

$$\Omega_0^2(0) = \frac{2\hbar U_0 k^2}{m}|\alpha_t|^2.$$

Note that the case of a control beam that significantly contributes to the optical trap that has been presented here has also already been published in [47, 48].

Cavity mode shape

Up to this point, we have neglected the mode shape of the TEM00 cavity mode (Fig. 2a, main text). The waist of the mode, however, depends on the position x_0 in the cavity. The maximum intensity of the standing wave along the TEM00 mode in the cavity is, accordingly, position dependent [55]:

$$I(x_0) = I_0 \frac{1}{1 + \frac{x_0^2}{x_R^2}},$$

note, that we have used here x_0 as the distance from the center of the cavity. It is related to the distance from the mirror x_0' by $x_0 = x_0' - \frac{L}{2}$ (x_R: Rayleigh length of the mode). Therefore, U_0 is an explicit function of the trap position x_0:

$$U_0(x_0) = \frac{\omega_{cav}\xi}{2\varepsilon_0 V_c}\left(1 + \frac{x_0^2}{x_R^2}\right)^{-1},$$

(ω_{cav}: laser frequency, ξ: particle polarizability, ε_0: vacuum permittivity, V_c: cavity mode volume). The polarizability of a particle is (see e.g. [13]):

$$\xi = 4\pi r^3 \varepsilon_0 \,\mathrm{Re}\left(\frac{\varepsilon - 1}{\varepsilon + 2}\right)$$

(ε: nanoparticle's dielectric constant; r: particle radius). In the main text we use these equations to determine the estimated particle size from $U_0(x_0)$, which is determined from the control beam power dependent coupling g_0(see main text, figure 3d) and the independently determied position of a particle in the cavity x_0(see appendix E).

Langevin Equations, effective frequency and damping

The Langevin equations for the mechanical quantum harmonic oscillator coupled to a thermal bath are:

$$\begin{aligned} \dot{\hat{x}}_m &= \frac{\hat{p}_m}{m} \\ \dot{\hat{p}}_m &= -m\Omega_0^2\hat{x}_m - \gamma_m\hat{p}_m + \sum_{j=t,c}\hbar\zeta_j\alpha_j(\hat{a}_j^\dagger + \hat{a}_j) + \eta(t), \end{aligned} \tag{A10}$$

where $\eta(t)$ is a thermal noise term, with the following correlation property [56]:

$$\langle \eta(t)\eta(t')\rangle = \frac{\gamma_m}{\Omega_0}\int \frac{d\omega}{2\pi}e^{-i\omega(t-t')}\omega \coth\left(\frac{\hbar\omega}{2k_BT}\right).$$

We assume that we are in a temperature range where $k_BT/\hbar \gg \Omega_0$:

$$\langle \eta(t)\eta(t')\rangle = \gamma_m \frac{2k_BT}{\hbar\Omega_0}\delta(t-t').$$

For the light beams, we can use the equations of motion as provided in equation A5 after the displacement of the light operators:

$$\begin{aligned}\dot{\hat{a}}_c &= -(\frac{\kappa}{2}+i\Delta)\hat{a}_c + i\zeta_c\alpha_c\hat{x}_m + \sqrt{\kappa}(\hat{c}_c^{in}+\hat{d}_c^{in}), \\ \dot{\hat{a}}_t &= -\frac{\kappa}{2}\hat{a}_t + i\zeta_t\alpha_t\hat{x}_m + \sqrt{\kappa}(\hat{c}_t^{in}+\hat{d}_t^{in})\end{aligned} \tag{A11}$$

By Fouriertransformation, we obtain a linear system of equations from which we retrieve the final expression for the position spectrum $S_{xx}(\omega)$ of levitating nanoparticles CM motion:

$$S_{xx} = \left|\chi_m^{\text{eff}}\right|^2 [S_{\text{th}} + S_{\text{rp}}],$$

where S_{th} is the thermal noise contribution and S_{rp} is the radiation-pressure contribution. In the regime our experiment is currently operating ($T = 293$ K; air pressure approx. 1-5 mbar), we expect that the thermal-noise contribution prevales:

$$S_{\text{th}} = X_{gs}^2\gamma_m\frac{2k_BT}{\hbar\Omega_0}$$

The effective susceptibility of the mechanical oscillator is

$$\chi_m^{\text{eff}} = \frac{\gamma_m}{(\Omega_{\text{eff}}(\omega)^2-\omega^2)^2 - i\gamma_{\text{eff}}(\omega)^2\omega^2}, \tag{A12}$$

where, following [56], we used the expressions:

$$\begin{aligned}\gamma_{\text{eff}}(\omega) &= \gamma_m - \frac{4g_0^2|\alpha_c|^2\Omega_0(\mu)\Delta\frac{\kappa}{2}}{\left(\left(\frac{\kappa}{2}\right)^2+(\omega+\Delta)^2\right)\left(\left(\frac{\kappa}{2}\right)^2+(\omega-\Delta)^2\right)} \\ \Omega_{\text{eff}}(\omega) &= \left[\Omega_0^2(\mu) + \frac{2g_0^2|\alpha_c|^2\Omega_0(\mu)\Delta\left[\left(\frac{\kappa}{2}\right)^2-\omega^2+\Delta^2\right]}{\left(\left(\frac{\kappa}{2}\right)^2+(\omega+\Delta)^2\right)\left(\left(\frac{\kappa}{2}\right)^2+(\omega-\Delta)^2\right)}\right]^{1/2}.\end{aligned}$$

Appendix B: Position readout by homodyne detection of the control beam

The expressions for the mechanical oscillator's dynamics, as well as its relationship to the control beam in the cavity, have been derived in the previous section (equations A10 and A11). In the following two sections, we will discuss how the mechanical oscillator position NPS is determined from the NPS obtained by homodyning of the control-beam phase signal in transmission of the cavity (see Methods M2 for implementation of homodyne detection).

We first derive the control light field in cavity transmission via the cavity input-output relation [57]:

$$\hat{d}_c^{out}(t) = \sqrt{\kappa}\hat{a}_c(t) - \hat{d}_c^{in}(t), \tag{B1}$$

where $\hat{d}_c^{in}$ describes the quantum noise at the cavity back mirror (i.e., the side from which the cavity is not driven). Even though our detection scheme occurs in two steps as described in the methods section, it is completely equivalent to a standard homodyne detection. The output signal is accordingly described by [58]:

$$s_{\text{opt}}(t) = \frac{1}{2}\left(|\hat{d}_c^{out}+\hat{a}_{LO}|^2 - |\hat{d}_c^{out}-\hat{a}_{LO}|^2\right) = \hat{d}_c^{out}\hat{a}_{LO}^* + \hat{d}_c^{out\dagger}\hat{a}_{LO}, \tag{B2}$$

where we describe the local oscillator by $\hat{a}_{LO}(t) = \alpha_{LO} \cdot e^{-i(\omega_c t+\theta)}$, where θ determines the detected quadrature of the control beam and α_{LO} is assumed to be real. In our experiment, the readout phase is locked to measure the phase quadrature: $\theta = \frac{\pi}{2}$.

From equations B1 and B2 we obtain:

$$\langle|\tilde{s}_{\mathrm{opt}}(\omega)|^2\rangle = \kappa\zeta_c^2\alpha_c^2 \left|\chi_c(\omega) + \chi_c^*(-\omega)\right|^2 S_{xx}(\omega)\delta(\omega), \tag{B3}$$

where we used the cavity susceptibility $\chi_c(\omega) = \frac{1}{\frac{\kappa}{2}-i(\omega-\Delta)}$. Up to a proportionality factor, Equation B3 resembles the result of the detection described in [49], and allows us to derive the mechanical NPS $S_{xx}(\omega)$ from the detected signal.

Appendix C: Data Evaluation and Temperature Calibration

To extract the mechanical NPS, we first measure the spectrum of the homodyne phase readout with and without particle for all values of μ and Δ. We obtain $\langle|\tilde{s}_{\mathrm{opt}}(\omega)|^2\rangle$ by substracting the background NPS (without particle) from the NPS with particle. To reconstruct the mechanical NPS S_{xx}, we need to account for the filtering by the Fabry-Perot cavity. We therefore divide $\langle|\tilde{s}_{\mathrm{opt}}(\omega)|^2\rangle$ by $|\chi_c(\omega) + \chi_c^*(-\omega)|^2$ following equation B3. The exact shape of S_{xx} is given by equation A12. To determine the effective frequency, damping and temperature we assume that we can describe the CM-motion of the particle as an harmonic oscillator, which is fulfilled as we are not operating in the strong coupling regime:

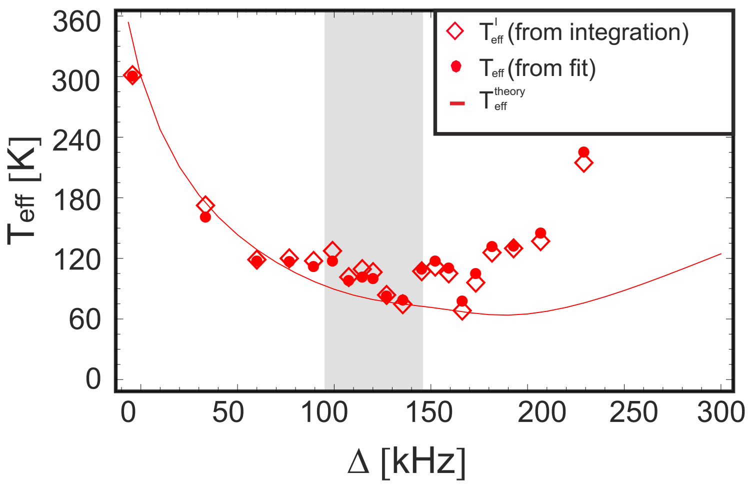

FIG. 4: **CM-motion temperature as a function of detuning.** The temperature of the CM-motion along the cavity axis as a function of detuning. The values are inferred via the equipartition theorem from the direct integration of the NPS (T^I_{eff},solid circles) and from the fitted spectra (T^*_{eff}, empty diamonds). The solid line shows the theoretical expectation $T^{\mathrm{theory}}_{\mathrm{eff}}(\Delta)$ infered from the detuning dependent frequency fit (optical spring; main text, Fig. 3).

$$f(\omega) = a \cdot T_{\mathrm{eff}} \cdot \frac{\gamma_{\mathrm{m}}}{(\omega^2 - \Omega^2_{\mathrm{eff}})^2 + \omega^2\gamma^2_{\mathrm{eff}}}. \tag{C1}$$

By fitting this model to S_{xx}, we obtain γ_{eff}, Ω_{eff} and T^*_{eff}. The calibration constant a is determined such that $T_{\mathrm{eff}} = 293\mathrm{K}$ in a particular measurement that was performed close to zero detuning ($\Delta = 1$ kHz for $\mu = 0.4$, blue NPS in Fig. 3, main text). This results in the values for the optical spring Ω_{eff} and damping γ_{eff} in Fig. 3, main text.

We can determine the optomechanical coupling g_0 from the the detuning dependence of Ω_{eff} for a given value of μ. However, we do not have an explicit analytical expression for this dependence. Instead, we apply the following strategy:

Using equation A12, we can calculate the optomechanical NPS S^{theory}_{xx} of our system for a given set of parameters (κ, g_0, Ω_0 and $\delta\Delta$). Here, $\delta\Delta$ is a systematic deviation from the detuning we set in the measurement: each value of Δ can be set precisely up to the uncertainty in the actual cavity resonance frequency. This frequency difference is accounted for with a joint offset $\delta\Delta$ in the values of Δ that is used as a fit parameter. We treat S^{theory}_{xx} in the same manner as the data and extract $\gamma^{\mathrm{theory}}_{\mathrm{eff}}$, $\Omega^{\mathrm{theory}}_{\mathrm{eff}}$ and $T^{\mathrm{theory}}_{\mathrm{eff}}$ by fitting $f(\omega)$ for each value of Δ. We use $\Omega^{\mathrm{theory}}_{\mathrm{eff}}(\Delta)$

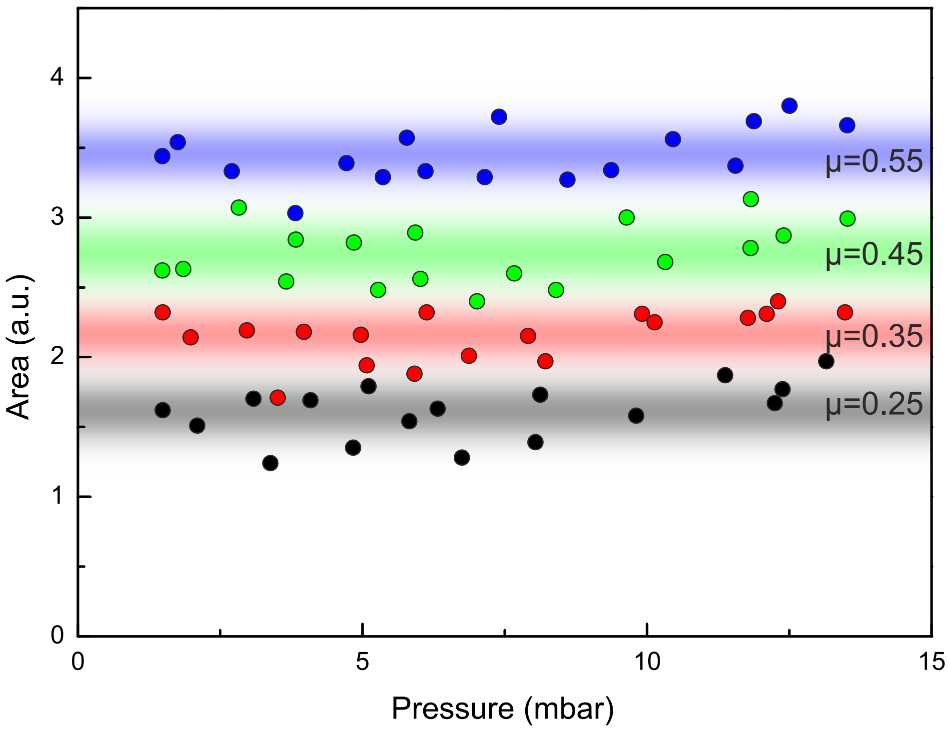

FIG. 5: Measurement of the NPS-area as a function of the ambient pressure. The data were taken for a resonant control beam. The area is proportional to the temperature of the CM motion of the nanoparticle for a given value of μ. It is independent of pressure indicating that the CM motion of the trapped nanoparticles is thermalized with the surrounding gas over the full measurement range. We conclude that the effective temperature of the CM mode is room temperature (293 K). The scatter of the data corresponds to an standard deviation of 5% for a temperature that is infered from the area of the NPS.

as a model that we fit to $\Omega_{\rm eff}$ optimizing the parameters g_0, Ω_0 and $\delta\omega$ in a least-square fit. The FWHM cavity line width κ is determined independently. The best fit parameters are used to obtain the theoretical dependences of $\gamma_{\rm eff}^{\rm theory}$ and $\Omega_{\rm eff}^{\rm theory}$ on the detuning shown in Fig. 3 in the main text and $T_{\rm eff}^{\rm theory}$ shown in Fig. 4.

The corresponding values of the predicted effective temperatures $T_{\rm eff}^{\rm theory}$ are shown in Fig. 4 along with the experimental data for $\mu = 0.4$. The latter is obtained in two ways: firstly as a free parameter $T_{\rm eff}^{*}$ in the fitted model $f(\omega)$ and secondly by direct integration over the measured NPS via $T_{\rm eff}^{I} = a^I \Omega_{\rm eff}^2 \int S_{xx} d\omega$. The calibration factor a^I is derived in the same way as a. The values $T_{\rm eff}^{*}$, obtained via fitting, agree well with those obtained by direct integration of the NPS. For small detunings Δ, the data follows the theoretical curve, while for larger detunings, heating unaccounted for in the theoretical model seems to occur. We are still investigating this effect, which may be due to laser noise. To obtain a good estimate of the minimal temperature achieved experimentally, we average the temperature obtained for a range of detunings $\Delta/2\pi \in [100, 150]$ kHz. The range is chosen such that the onset of temperature increase is not yet strong and the predicted range of $T_{\rm eff}$ is small compared to the distribution of measured temperatures. The experimental data in Fig. 3e in the main text is obtained by applying this evaluation for the different values of μ for $T_{\rm eff}^{I}$ obtained by direct integration. The theory curve in Fig. 3e in the main text is obtained by averaging the theoretical prediction for $T_{\rm eff}^{\rm theory}$ over the same range of detunings $\Delta/2\pi \in [100, 150]$ kHz.

Appendix D: Kinetic gas theory - Pressure-dependent damping

The pressure dependence of the damping for a trapped nanosphere is given by [21, 22, 59] :

$$\gamma_0 = \frac{6\pi\eta r}{m} \frac{0.619}{0.619 + Kn}(1 + c_{\rm k}) \tag{D1}$$

where η is the viscosity coefficient for air, r and m are the radius and mass of the nanosphere, $Kn = \lambda_{\rm fp}/r$ is the Knudsen number and $\lambda_{\rm fp}$ is the mean free path for air particles. $c_{\rm k} = 0.31Kn/(0.785 + 1.152Kn + Kn^2)$ is a small correction factor necessary at higher pressures [59]. Figure 2b in the main text shows a pressure dependent damping measurement, where the control beam is used just for readout (i.e. μ=0.1, resonant).

Figure 5 shows the temperature associated with the CM motion of the particle as a function of pressure. At high pressures, the nanoparticle experiences more collisions with the gas resulting in a stronger damping of its CM motion. If the nanoparticle CM motion was not thermalized at low pressures due to a heating process, better thermalization and therefore lower temperatures would be expected at higher pressures due to the increased damping rate. As Fig. 5 shows a constant CM motion temperature for the different pressures and values of μ, we conclude it is thermalized with the environment in all these measurements, which implies a temperature of 293K as long as no optical damping is introduced.

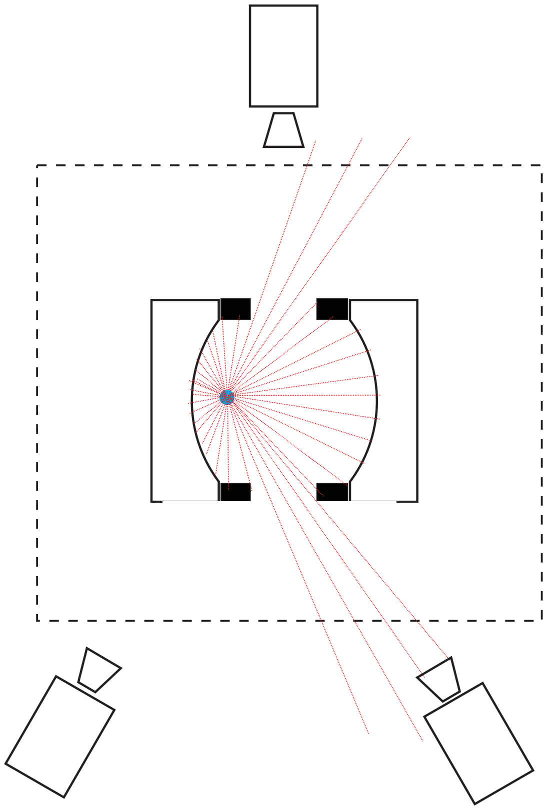

FIG. 6: **Schematic of the configuration of the CCD imaging setup**. We use a combination of three CCD cameras to observe and locate the particle. This configuration allows access to a larger range of positions along the cavity axis compared to a single camera. Based on the pictures of the CCD cameras, we determine the position x_0 of a particle in the cavity.

Appendix E: Position detection

Three cameras with achromatic lenses monitor the cavity and image the light scattered off trapped nanoparticles. As can be seen in Figure 1a of the main text, the black retaining rings and the concave shape of the mirrors prevent optical access over the whole cavity length from a single point of view. We use a configuration of three CCD cameras, as shown in figure 6, to extend the field of view. By combining the images from the 3 cameras, we can reconstruct a larger field of view. To determine the position of the particle from the image, we need to calibrate the coordinates. To this end, the mechanical frequency at several positions is measured along with the position of a particle on the CCD image. This measurement is repeated for several particles. The frequency dependence on position allows calibrating the camera.

The mode shape in the optical cavity is well-known from the curvature of the mirrors and the cavity length, which is determined with high precision from the FSR. The expected longitudinal frequency dependence of a nanoparticle trapped in the standing wave is $\Omega_0 = \Omega_c \frac{1}{\sqrt{1+((x_0-x_c)/x_R)^2}}$ (x_c: cavity center position, Ω_c: frequency at position x_c; x_R: Rayleigh length of the Gaussian mode). The measured mechanical frequencies for several different trap positions of the same nanoparticle and the corresponding coordinates ζ (in pixels) on the camera images are fitted to the function $\Omega_0 = \Omega_c \frac{1}{\sqrt{1+((\zeta-\zeta_c)\xi/x_R)^2}}$ with fit parameters ζ_c (coordinate of the center of the cavity in pixels), ξ (conversion factor between pixels and millimeters) and Ω_c (mechanical frequency in the center of the cavity). A corresponding measurement for one nanoparticle with calibrated length scale is shown in the main text, figure 2b. Based on this calibration we determine the position of the nanoparticle used in the measurements summarized in Fig. 3. It is located at a distance $x_0' = 3.92 \pm 0.14$ mm from the cavity mirror, i.e. at a distance $x_0 = 1.56 \pm 0.14$ mm from the center of the cavity.

---

[1] R. Blatt and C. F. Roos, Nature Physics **8**, 277 (2012).
[2] I. Bloch, J. Dalibard, and S. Nascimbène, Nature Physics **8**, 267 (2012).
[3] H. Haffner, R. C., and R. Blatt, Physics Reports **469**, 155 (2008).
[4] D. Kielpinski, C. Monroe, and D. J. Wineland, Nature **417**, 709 (2002).
[5] H. J. Kimble, Nature **453**, 1023 (2008).
[6] S. Ritter, C. Nölleke, C. Hahn, A. Reiserer, A. Neuzner, M. Uphoff, M. Mücke, E. Figueroa, J. Bochmann, and G. Rempe, Nature **484**, 195 (2012).
[7] A. Stute, B. Casabone, B. Brandstatter, K. Friebe, T. E., Northup, and R. Blatt, Nat Photon **7**, 219 (2013).
[8] J. Hofmann, M. Krug, N. Ortegel, L. Gérard, M. Weber, W. Rosenfeld, and H. Weinfurter, Science **337**, 72 (2012).
[9] S. Gerlich, S. Eibenberger, M. Tomandl, S. Nimmrichter, K. Hornberger, P. J. Fagan, J. Tüxen, M. Mayor, and M. Arndt, Nature Communications **2**, 263 (2011).
[10] K. Hornberger, S. Gerlich, P. Haslinger, S. Nimmrichter, and M. Arndt, Reviews of Modern Physics **84**, 157 (2012).
[11] M. Aspelmeyer, P. Meystre, and K. Schwab, Physics Today **65**, 29 (2012).
[12] M. Aspelmeyer, T. Kippenberg, and F. Marquardt, arXiv:1303.0733v1 (2013).
[13] D. E. Chang, C. A. Regal, S. B. Papp, D. J. Wilson, J. Ye, O. Painter, H. J. Kimble, and P. Zoller, Proceedings of the National Academy of Sciences of the United States of America **107**, 1005 (2010).
[14] O. Romero-Isart, M. L. Juan, R. Quidant, and J. I. Cirac, New Journal of Physics **12**, 033015 (2010).
[15] O. Romero-Isart, A. C. Pflanzer, F. Blaser, R. Kaltenbaek, N. Kiesel, M. Aspelmeyer, and J. I. Cirac, PRL **107**, 020405 (2011).
[16] A. Geraci, S. Papp, and J. Kitching, Phys. Rev. Lett. **105**, 101101 (2010).
[17] A. Arvanitaki and A. A. Geraci, Phys. Rev. Lett. **110**, 071105 (2013).
[18] P. Horak, G. Hechenblaikner, K. Gheri, H. Stecher, and H. Ritsch, Physical Review Letters **79**, 4974 (1997).
[19] V. Vuletić and S. Chu, Physical Review Letters **84**, 3787 (2000).
[20] A. Ashkin and J. M. Dziedzic, Applied Physics Letters **30**, 202 (1977).
[21] T. Li, S. Kheifets, and M. G. Raizen, Nat Phys **7**, 527 (2011).
[22] J. Gieseler, B. Deutsch, R. Quidant, and L. Novotny, Physical Review Letters **109**, 103603 (2012).
[23] M. Koch, C. Sames, A. Kubanek, M. Apel, M. Balbach, A. Ourjoumtsev, P. Pinkse, and G. Rempe, Physical Review Letters **105**, 173003 (2010).
[24] J. Ye, D. W. Vernooy, and H. J. Kimble, Physical Review Letters **83**, 4987 (1999).
[25] J. McKeever, J. R. Buck, A. D. Boozer, A. Kuzmich, H.-C. Nägerl, D. M. Stamper-Kurn, and H. J. Kimble, Physical Review Letters **90**, 2 (2003).
[26] P. Maunz, T. Puppe, I. Schuster, N. Syassen, P. W. H. Pinkse, and G. Rempe, Nature **428**, 50 (2004).
[27] D. R. Leibrandt, J. Labaziewicz, V. Vuletic, and I. L. Chuang, Phys. Rev. Lett. **103**, 103001 (2009).
[28] A. Stute, B. Casabone, P. Schindler, T. Monz, P. O. Schmidt, B. Brandstatter, T. E. Northup, and R. Blatt, Nature **485**, 482 (2012).
[29] G. Hechenblaikner, M. Gangl, P. Horak, and H. Ritsch, Physical Review A **58**, 3030 (1998).
[30] M. Gangl and H. Ritsch, European Physical Journal D **8**, 29 (2000).
[31] I. Favero, S. Stapfner, D. Hunger, P. Paulitschke, J. Reichel, H. Lorenz, E. M. Weig, and K. Karrai, Optics Express **17**, 16 (2009).
[32] G. Anetsberger, O. Arcizet, Q. P. Unterreithmeier, R. Rivière, A. Schliesser, E. M. Weig, Kotthaus, J. P., and T. J. Kippenberg, Nature Physics **5**, 909 (2009).
[33] J. Chan, T. P. M. Alegre, A. H. Safavi-Naeini, J. T. Hill, A. Krause, S. Gröblacher, M. Aspelmeyer, and O. Painter, Nature **478**, 89 (2011).
[34] J. D. Thompson, B. M. Zwickl, A. M. Jayich, F. Marquardt, S. M. Girvin, and J. G. E. Harris, Nature **452**, 72 (2008).
[35] J. D. Teufel, T. Donner, D. Li, J. W. Harlow, M. S. Allman, K. Cicak, A. J. Sirois, J. D. Whittaker, K. W. Lehnert, and R. W. Simmonds, Nature **475**, 359 (2011).
[36] T. P. Purdy, R. W. Peterson, and C. A. Regal, Science **339**, 801 (2013).
[37] A. H. Safavi-Naeini, J. Chan, J. T. Hill, T. P. Mayer Alegre, A. Krause, and O. Painter, Phys. Rev. Lett. **108**, 033602 (2012).
[38] K. W. Murch, K. L. Moore, S. Gupta, and D. M. Stamper-Kurn, Nature Physics **4**, 561 (2008).
[39] T. Purdy, D. Brooks, T. Botter, N. Brahms, Z.-Y. Ma, and D. M. Stamper-Kurn, Phys. Rev. Lett. **105**, 133602 (2010).

[40] M. H. Schleier-Smith, I. D. Leroux, H. Zhang, M. A. Van Camp, and V. Vuletić, Physical Review Letters **107**, 143005 (2011).
[41] R. Kaltenbaek, G. Hechenblaikner, N. Kiesel, O. Romero-Isart, K. Schwab, U. Johann, and M. Aspelmeyer, Experimental Astronomy **34**, 123 (2012).
[42] A. Ashkin, *Optical trapping and manipulation of neutral particles using lasers* (World Scientific Pub Co, 2007).
[43] S. Nimmrichter, K. Hammerer, P. Asenbaum, H. Ritsch, and M. Arndt, New Journal of Physics **12**, 083003 (2010).
[44] O. Romero-Isart, A. Pflanzer, M. Juan, R. Quidant, N. Kiesel, M. Aspelmeyer, and J. I. Cirac, Phys. Rev. A **83**, 013803 (2011).
[45] P. F. Barker and M. N. Shneider, Phys. Rev. A **81**, 023826 (2010).
[46] D. Stamper-Kurn, arXiv:1204.4351v1 (2012).
[47] G. A. T. Pender, P. F. Barker, F. Marquardt, J. Millen, and T. S. Monteiro, Phys. Rev. A **85**, 021802 (2012).
[48] T. S. Monteiro, J. Millen, G. A. T. Pender, F. Marquardt, D. Chang, and P. F. Barker, New Journal of Physics **15**, 015001 (2013).
[49] M. Paternostro, S. Gigan, M. S. Kim, F. Blaser, H. R. Böhm, and M. Aspelmeyer, New Journal of Physics **8**, 107 (2006).
[50] A. Ashkin and J. M. Dziedzic, Applied Physics Letters **28**, 333 (1976).
[51] U. Akram, N. Kiesel, M. Aspelmeyer, and G. J. Milburn, New Journal of Physics **12**, 083030 (2010).
[52] O. Romero-Isart, Phys. Rev. A **84**, 052121 (2011).
[53] W. Lechner, S. J. M. Habraken, N. Kiesel, M. Aspelmeyer, and P. Zoller, Phys. Rev. Lett. **110**, 143604 (2013).
[54] M. D. Summers, D. R. Burnham, and D. McGloin, Optics Express **16**, 7739 (2008).
[55] B. E. A. Saleh and M. C. Teich, *Fundamentals of photonics* (Wiley-Interscience, 2007).
[56] C. Genes, D. Vitali, P. Tombesi, S. Gigan, and M. Aspelmeyer, Physical Review A **77**, 33804 (2008).
[57] C. Gardiner and P. Zoller, *Quantum noise: a handbook of Markovian and non-Markovian quantum stochastic methods with applications to quantum optics*, vol. 56 (Springer, 2004).
[58] H.-A. Bachor and T. C. Ralph, *A Guide to Experiments in Quantum Optics* (Wiley-VCH, 2004).
[59] S. A. Beresnev, V. G. Chernyak, and G. A. Fomyagin, Journal of Fluid Mechanics **219**, 405 (1990).

9 Bibliography

[1] M. Aspelmeyer, T. J. Kippenberg, and F. Marquardt, "Cavity Optomechanics," *ArXiv e-prints*, Mar. 2013.

[2] J. D. Teufel, T. Donner, D. Li, J. W. Harlow, M. S. Allman, K. Cicak, A. J. Sirois, J. D. Whittaker, K. W. Lehnert, and R. W. Simmonds, "Sideband cooling of micromechanical motion to the quantum ground state," *Nature*, vol. 475, pp. 359–363, July 2011.

[3] J. Chan, T. P. M. Alegre, A. H. Safavi-Naeini, J. T. Hill, A. Krause, S. Gröblacher, M. Aspelmeyer, and O. Painter, "Laser cooling of a nanomechanical oscillator into its quantum ground state," *Nature*, vol. 478, pp. 89–92, Oct. 2011.

[4] E. Schrödinger, "Die gegenwärtige situation in der quantenmechanik," *Naturwissenschaften*, vol. 23, no. 49, pp. 823–828, 1935.

[5] T. Aoki, B. Dayan, E. Wilcut, W. P. Bowen, A. S. Parkins, T. J. Kippenberg, K. J. Vahala, and H. J. Kimble, "Observation of strong coupling between one atom and a monolithic microresonator," *Nature*, vol. 443, pp. 671–674, Oct. 2006.

[6] J. D. Teufel, D. Li, M. S. Allman, K. Cicak, A. J. Sirois, J. D. Whittaker, and R. W. Simmonds, "Circuit cavity electromechanics in the strong-coupling regime," *Nature*, vol. 471, pp. 204–208, Mar. 2011.

[7] S. Gröblacher, K. Hammerer, M. R. Vanner, and M. Aspelmeyer, "Observation of strong coupling between a micromechanical resonator and an optical cavity field," *Nature*, vol. 460, pp. 724–727, Aug. 2009.

[8] T. A. Palomaki, J. W. Harlow, J. D. Teufel, R. W. Simmonds, and K. W. Lehnert, "Coherent state transfer between itinerant microwave fields and a mechanical oscillator," *Nature*, vol. 495, pp. 210–214, Mar. 2013.

[9] X. Wang, S. Vinjanampathy, F. W. Strauch, and K. Jacobs, "Ultraefficient Cooling of Resonators: Beating Sideband Cooling with Quantum Control," *Physical Review Letters*, vol. 107, p. 177204, Oct. 2011.

[10] K. W. Murch, K. Moore, S. Gupta, and D.-M. Stamper-Kurn, "Observation of quantum-measurement backaction with an ultracold atomic gas," *Nat.Phys.*, vol. 4, pp. 561–564, Nov. 2008.

[11] M. H. Schleier-Smith, I. D. Leroux, H. Zhang, M. A. van Camp, and V. Vuletić, "Optomechanical Cavity Cooling of an Atomic Ensemble," *Physical Review Letters*, vol. 107, p. 143005, Sept. 2011.

[12] A. Schliesser, P. Del'Haye, N. Nooshi, K. J. Vahala, and T. J. Kippenberg, "Radiation Pressure Cooling of a Micromechanical Oscillator Using Dynamical Backaction," *Physical Review Letters*, vol. 97, p. 243905, Dec. 2006.

[13] J. D. Thompson, B. M. Zwickl, A. M. Jayich, F. Marquardt, S. M. Girvin, and J. G. E. Harris, "Strong dispersive coupling of a high-finesse cavity to a micromechanical membrane," *Nature*, vol. 452, pp. 72–75, Mar. 2008.

[14] S. Gigan, H. R. Böhm, M. Paternostro, F. Blaser, G. Langer, J. B. Hertzberg, K. C. Schwab, D. Bäuerle, M. Aspelmeyer, and A. Zeilinger, "Self-cooling of a micromirror by radiation pressure," *Nature*, vol. 444, pp. 67–70, Nov. 2006.

[15] O. Arcizet, P.-F. Cohadon, T. Briant, M. Pinard, and A. Heidmann, "Radiation-pressure cooling and optomechanical instability of a micromirror," *Nature*, vol. 444, pp. 71–74, Nov. 2006.

[16] O. Romero-Isart, M. L. Juan, R. Quidant, and J. I. Cirac, "Toward quantum superposition of living organisms," *New Journal of Physics*, vol. 12, p. 033015, Mar. 2010.

[17] D. E. Chang, C. A. Regal, S. B. Papp, D. J. Wilson, J. Ye, O. Painter, H. J. Kimble, and P. Zoller, "Cavity opto-mechanics using an optically levitated nanosphere," *Proceedings of the National Academy of Science*, vol. 107, pp. 1005–1010, Jan. 2010.

[18] P. F. Barker, "Doppler Cooling a Microsphere," *Physical Review Letters*, vol. 105, p. 073002, Aug. 2010.

[19] T. S. Monteiro, J. Millen, G. A. T. Pender, F. Marquardt, D. Chang, and P. F. Barker, "Dynamics of levitated nanospheres: towards the strong coupling regime," *New Journal of Physics*, vol. 15, p. 015001, Jan. 2013.

[20] N. Kiesel, F. Blaser, U. Delić, D. Grass, R. Kaltenbaek, and M. Aspelmeyer, "Cavity cooling of an optically levitated nanoparticle," *ArXiv e-prints*, Apr. 2013.

[21] A. A. Gilbert Grynberg and C. Fabre, *Introduction to Quantum Optics.* New York: Cambridge University Press, 2010.

[22] B. Saleh and M. Teich, *Fundamentals of Photonics.* Wiley-Interscience, second ed., 2007.

[23] R. Loudon, *The Quantum Theory of Light.* New York: Oxford University Press, third ed., 2000.

[24] D. Walls and G. J. Milburn, *Quantum Optics.* Springer, second ed., 2008.

[25] S. Nimmrichter, K. Hammerer, P. Asenbaum, H. Ritsch, and M. Arndt, "Master equation for the motion of a polarizable particle in a multimode cavity," *New Journal of Physics*, vol. 12, p. 083003, Aug. 2010.

[26] C. Genes, D. Vitali, P. Tombesi, S. Gigan, and M. Aspelmeyer, "Ground-state cooling of a micromechanical oscillator: Comparing cold damping and cavity-assisted cooling schemes," *Phys. Rev. A*, vol. 77, p. 033804, Mar. 2008.

[27] C. Gardiner and P. Zoller, *Quantum noise: a handbook of Markovian and non-Markovian quantum stochastic methods with applications to quantum optics*, vol. 56. Springer, 2004.

[28] J. B. Hagen, *Radio-Frequency Electronics.* New York: Cambridge University Press, second ed., 2009.

[29] M. Paternostro, S. Gigan, M. S. Kim, F. Blaser, H. R. Böhm, and M. Aspelmeyer, "Reconstructing the dynamics of a movable mirror in a detuned optical cavity," *New Journal of Physics*, vol. 8, p. 107, June 2006.

[30] A. M. Jayich, J. C. Sankey, K. Børkje, D. Lee, C. Yang, M. Underwood, L. Childress, A. Petrenko, S. M. Girvin, and J. G. E. Harris, "Cryogenic optomechanics with a Si_3N_4 membrane and classical laser noise," *New Journal of Physics*, vol. 14, p. 115018, Nov. 2012.

[31] A. H. Safavi-Naeini, J. Chan, J. T. Hill, S. Gröblacher, H. Miao, Y. Chen, M. Aspelmeyer, and O. Painter, "Laser noise in cavity-optomechanical cooling and thermometry," *New Journal of Physics*, vol. 15, p. 035007, Mar. 2013.

[32] A. A. Clerk, M. H. Devoret, S. M. Girvin, F. Marquardt, and R. J. Schoelkopf, "Introduction to quantum noise, measurement, and amplification," *Reviews of Modern Physics*, vol. 82, pp. 1155–1208, Apr. 2010.

[33] M. Lax and W. Cai, *Random Processes in Physics and Finance.* New York: Oxford University Press, ninth dover printing, tenth gpo printing ed., 2006.

[34] J. D. Jackson, *Classical Electrodynamics*. Wiley, third ed., 1999.

10 List of Figures

Curriculum Vitae

Uroš Delić

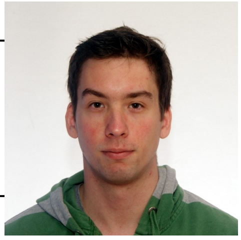

EDUCATION

- 2012 – University of Vienna, Faculty of Physics, Master degree programme
  GPA 1.27 (scale 1-4, 1 denoting the highest grade).
- 2012 University of Vienna, Faculty of Physics, Bachelor degree programme
  GPA 1.10 (scale 1-4, 1 denoting the highest grade), graduated with distinction
- 2006 – 2010 University of Belgrade, Faculty of Physics, Bachelor degree programme
  Course: *Theoretical and Experimental Physics*
  GPA 9.82 (scale 6-10, 10 denoting the highest grade), full scholarship
- 2006 – Union University, School of Computing, Bachelor's degree studies
  Course: *Computer sciences*
  GPA 8.95 (scale 6-10, 10 denoting the highest grade), full scholarship
- 2002 – 2006 High school of Mathematics, Belgrade, Serbia
  Elite high school for gifted students, GPA 5.00 (scale 2-5, 5 denoting the highest grade)

RESEARCH EXPERIENCE

- 11.2009 – Scientific research in the group of Univ. Prof. Dr. Markus Aspelmeyer at the University of Vienna, working on experiments in quantum optomechanics.
- 05.2009 – 07.2009 Internship at the Research Laboratory of Electronics, Massachusetts Institute of Technology, under the supervision of Prof. Dr. Vladan Vuletić
  Project details: *Design and production of electronics (current and voltage controllers, PID boxes) necessary for the experiment on trapping of atoms, building and calibrating a diode laser*
- 10.2007 One-month internship at Delayed choice experimental group of Dr. Thomas Jenewein at the Institute for Quantum Optics and Quantum Information, Vienna, Austria
  Project details: *Production of an interferometer needed for the Delayed choice experiment. Working on the software for coincidence statistics evaluation*
- 03.2005 – 12.2005 Petnica Science Center, Valjevo and Institute of Physics, Belgrade, Serbia
  Project: *Simulations of formation and evolution of planets*
- 03.2004 – 12.2004 Petnica Science Center, Valjevo, Serbia
  Project: *Chaos in dripping water*

VOLUNTEER EXPERIENCE

- 03.2009 – 05.2009 Ministry of Science and Technological Development
  Working on the Strategy of Scientific and Technological development of the Republic of Serbia for the period from 2009. to 2014.
- 2008 - 2009 Organization "Museum night"
  Coordinator of Physics' exhibition at Science Festivals in Belgrade

- 2008 – 2009 Member of the Scientific Committee of the University of Belgrade, President of the Center for scientific and research work of students at the Faculty of Physics
  Working on connecting professors and students and affording an opportunity to students to do practical work in research groups at the Faculty of Physics.
- 2007 - 2009 High School of Computing and Mathematical High School
  Professor of physics, mainly preparing students for high school competitions
- 2007 - Petnica Science Center, Valjevo, Serbia
  Teaching associate (giving lectures in different topics from physics and mentoring different physics' projects)

COMPETITIONS AND AWARDS

- December 2009 Eurobank EFG Scholarship to the 100 Best Serbian Students
- December 2006 Prize for wining the bronze medal at the International Physics Olympiad from the Fund for young talents, Serbia
- July 2006 International Physics Olympiad, Singapore, July 2006 *Bronze Medal*
- October 2004 International Astronomical Olympiad, Simeiz, Ukraine *Bronze Medal*

SCHOLARSHIPS

- 10.2013 - CoQuS Scholarship
- 2007 - 2010 Scholarship of the Ministry of Science and Technological Development
- 2006 - 2010 Full undergraduate scholarship from the Faculty of Physics, University of Belgrade
- 2006 - 2010 Full undergraduate scholarship from the Union University School of Computing
- 2005 - 2006 Scholarship of the City of Belgrade
- 2004 Republic Foundation for the Encouragement of Scientific and Artistic Youth